Supplementary Materials

Daily to centennial behavior of aseismic slip along the central section of the North Anatolian Fault

R. Jolivet[1,2], J. Jara[1], M. Dalaison[1], B. Rouet-Leduc[3], A. Özdemir[4], U. Dogan[4], Z. Çakir[5], S. Ergintav[6]& P. Dubernet[1]

[1]Laboratoire de Géologie, Département de Géosciences, École Normale Supérieure, PSL Université, CNRS UMR 8538, Paris, France

[2]Institut Universitaire de France, 1 rue Descartes, 75006 Paris

[3]Disaster Prevention Research Institute, Kyoto University, Kyoto, Japan

[4] Department of Geomatic Engineering, Yildiz Technical University, 34220 Istanbul, Turkey

[5]Department of Geology, Istanbul Technical University, 34469 Istanbul, Turkey

[6]Department of Geodesy, Kandilli Observatory and Earthquake Research Institute, Bogazici University, 34684 Istanbul, Turkey

Contents of this file

1. InSAR data complementary figures

1.1. InSAR dataset

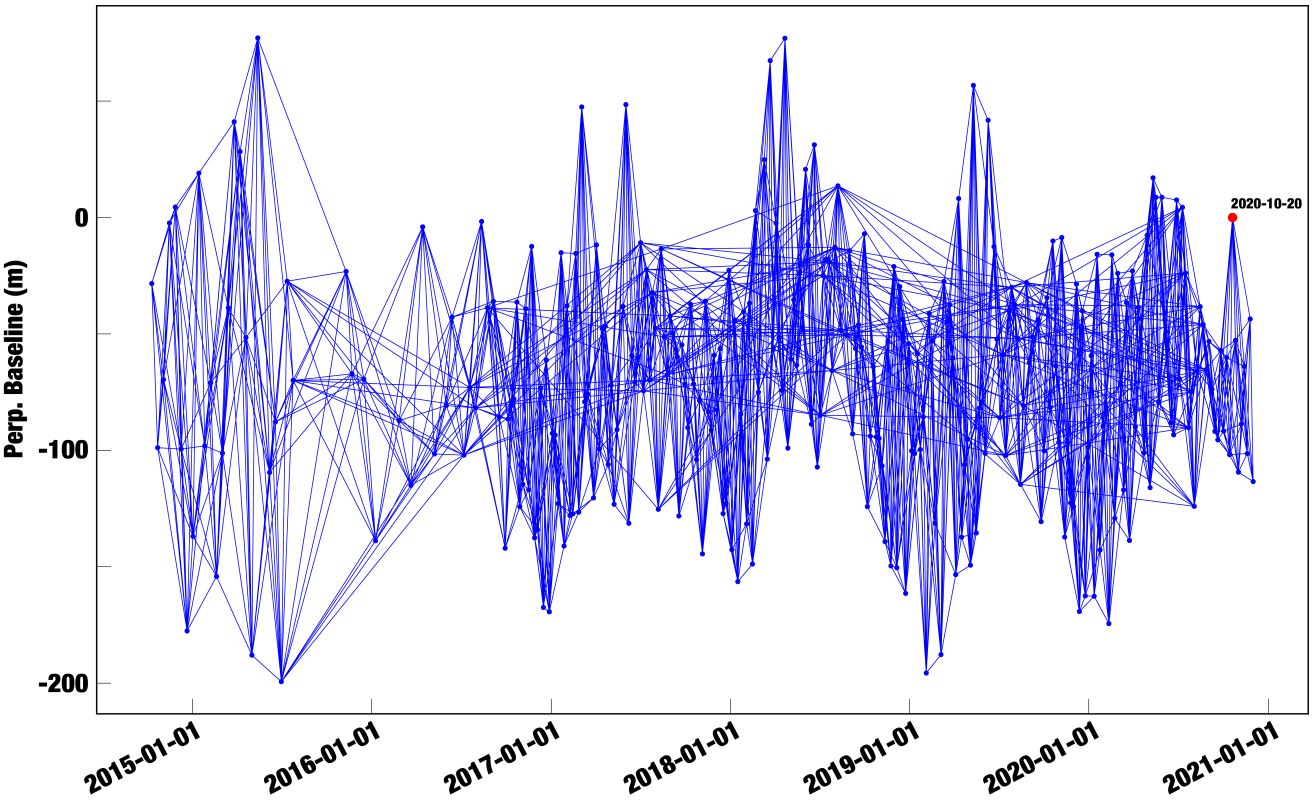

Figure S-1. Perpendicular baseline as a function of acquisition dates for track 65 - Blue dots represent the perpendicular baseline at the date of each acquisition by the Sentinel 1 A and B satellites. Red dot is the image chosen as reference for the geometry. Blue lines are the interferograms we computed.

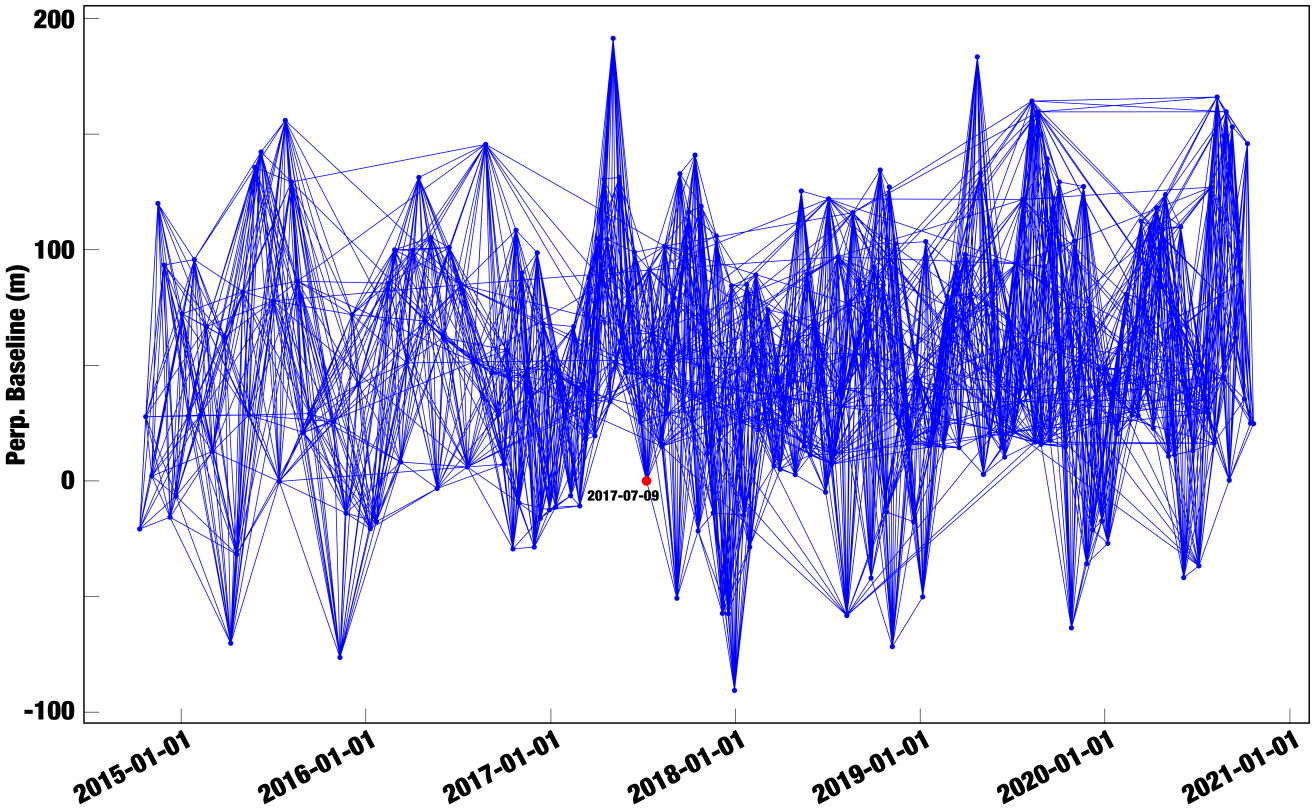

Figure S-2. Perpendicular baseline as a function of acquisition dates for track 87 - Blue dots represent the perpendicular baseline at the date of each acquisition by the Sentinel 1 A and B satellites. Red dot is the image chosen as reference for the geometry. Blue lines are the interferograms we computed.

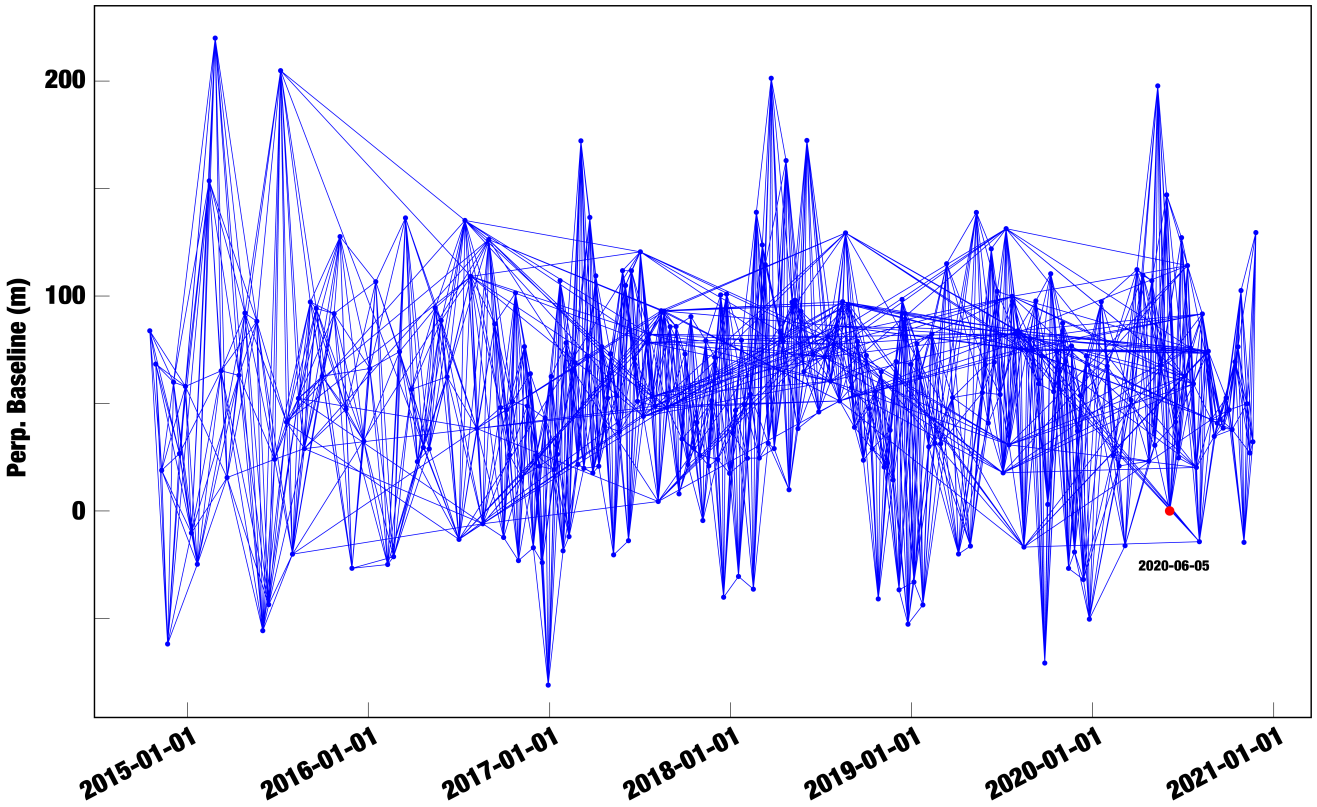

Figure S-3. Perpendicular baseline as a function of acquisition dates for track 167- Blue dots represent the perpendicular baseline at the date of each acquisition by the Sentinel 1 A and B satellites. Red dot is the image chosen as reference for the geometry. Blue lines are the interferograms we computed.

1.2. Full velocity maps

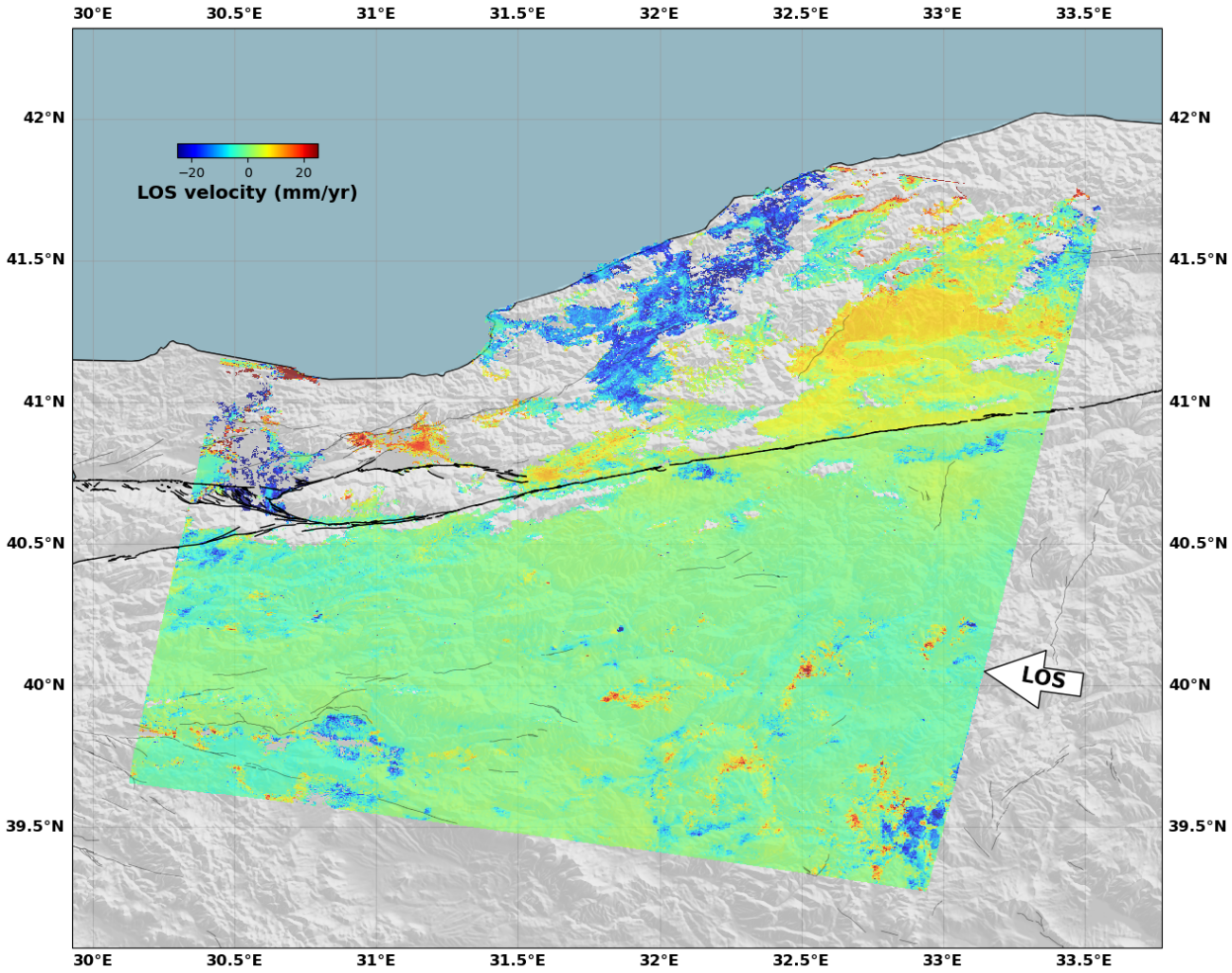

Figure S-4. Line-of-sight velocity map from track 65 - Velocity map computed from the time series of InSAR data on track 65. All available pixels are shown.

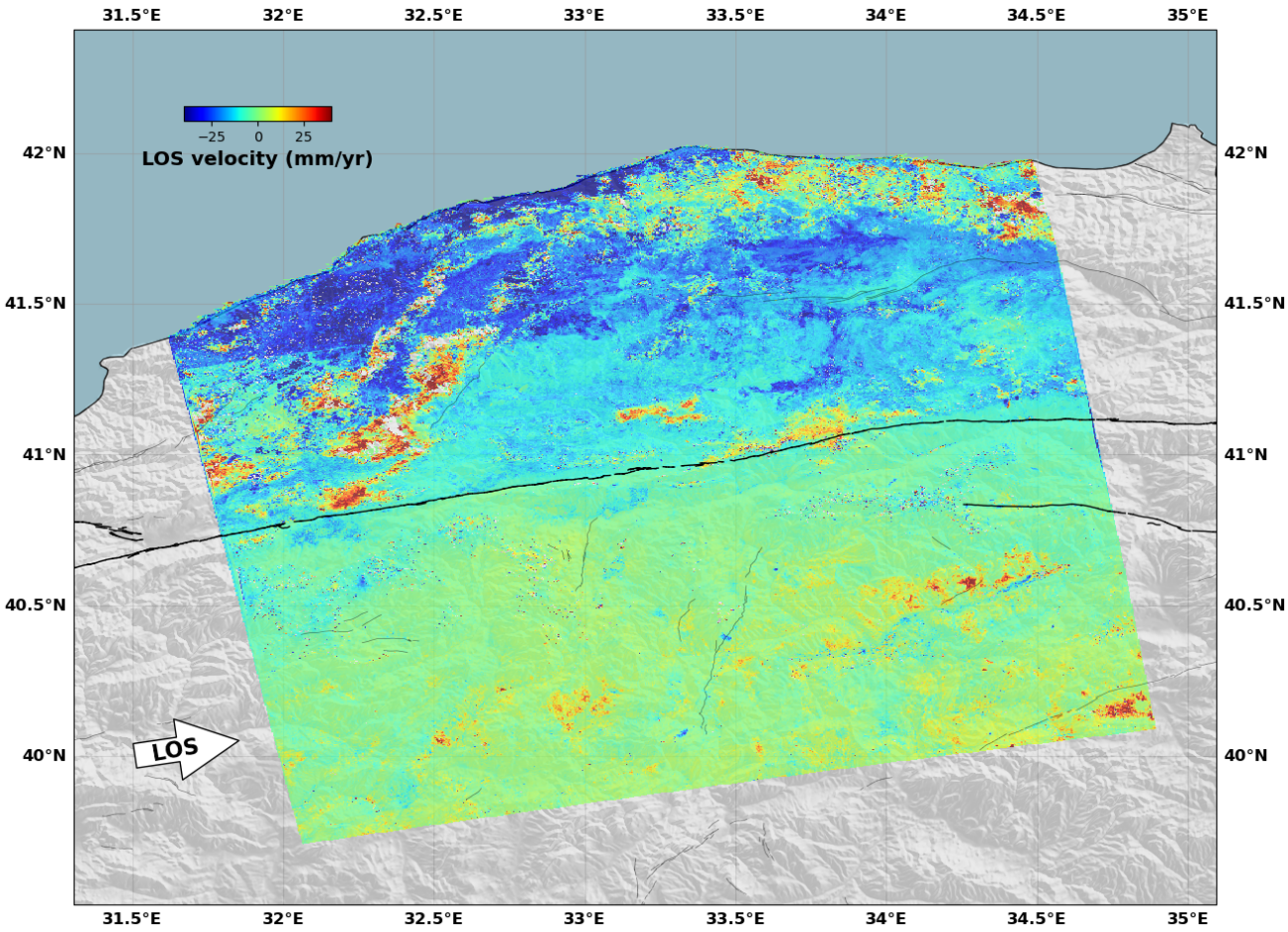

Figure S-5. Line-of-sight velocity map from track 87 - Velocity map computed from the time series of InSAR data on track 87. All available pixels are shown.

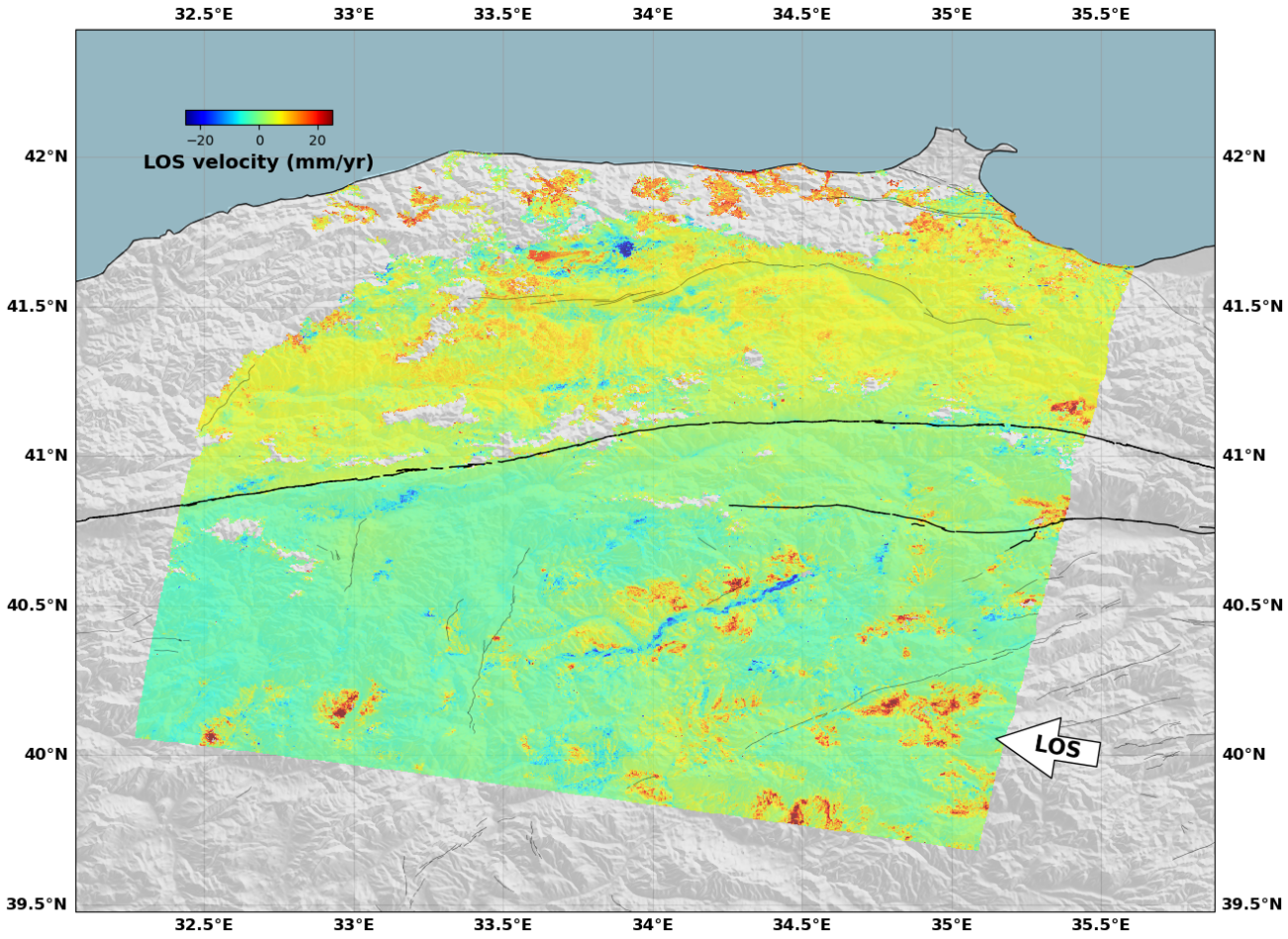

Figure S-6. Line-of-sight velocity map from track 167 - Velocity map computed from the time series of InSAR data on track 167. All available pixels are shown.

1.3. Velocity standard deviation maps

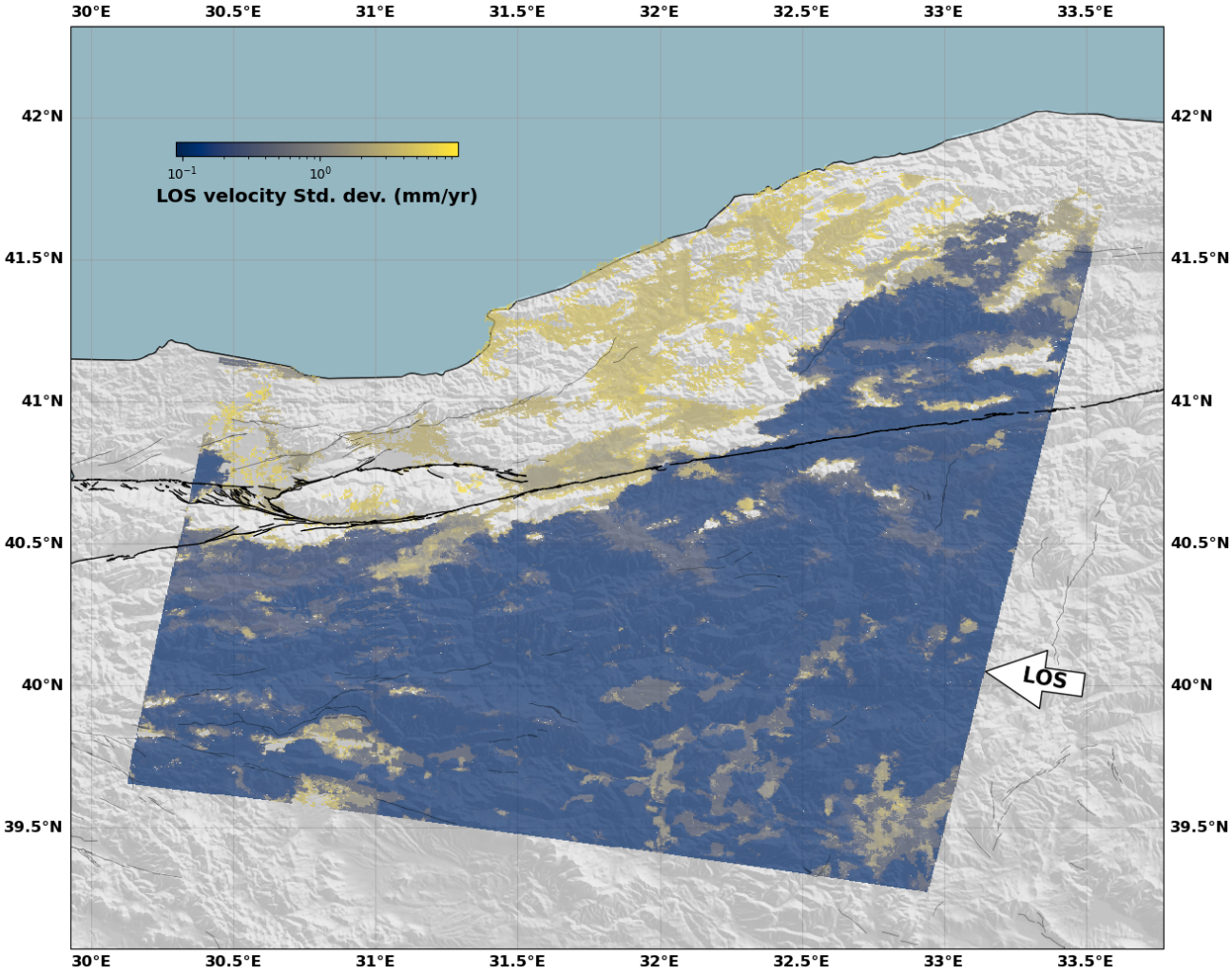

Figure S-7. Line-of-sight velocity standard deviation map from track 65 - Standard deviations are from the analyzed state covariance at the end of the Kalman filtering procedure.

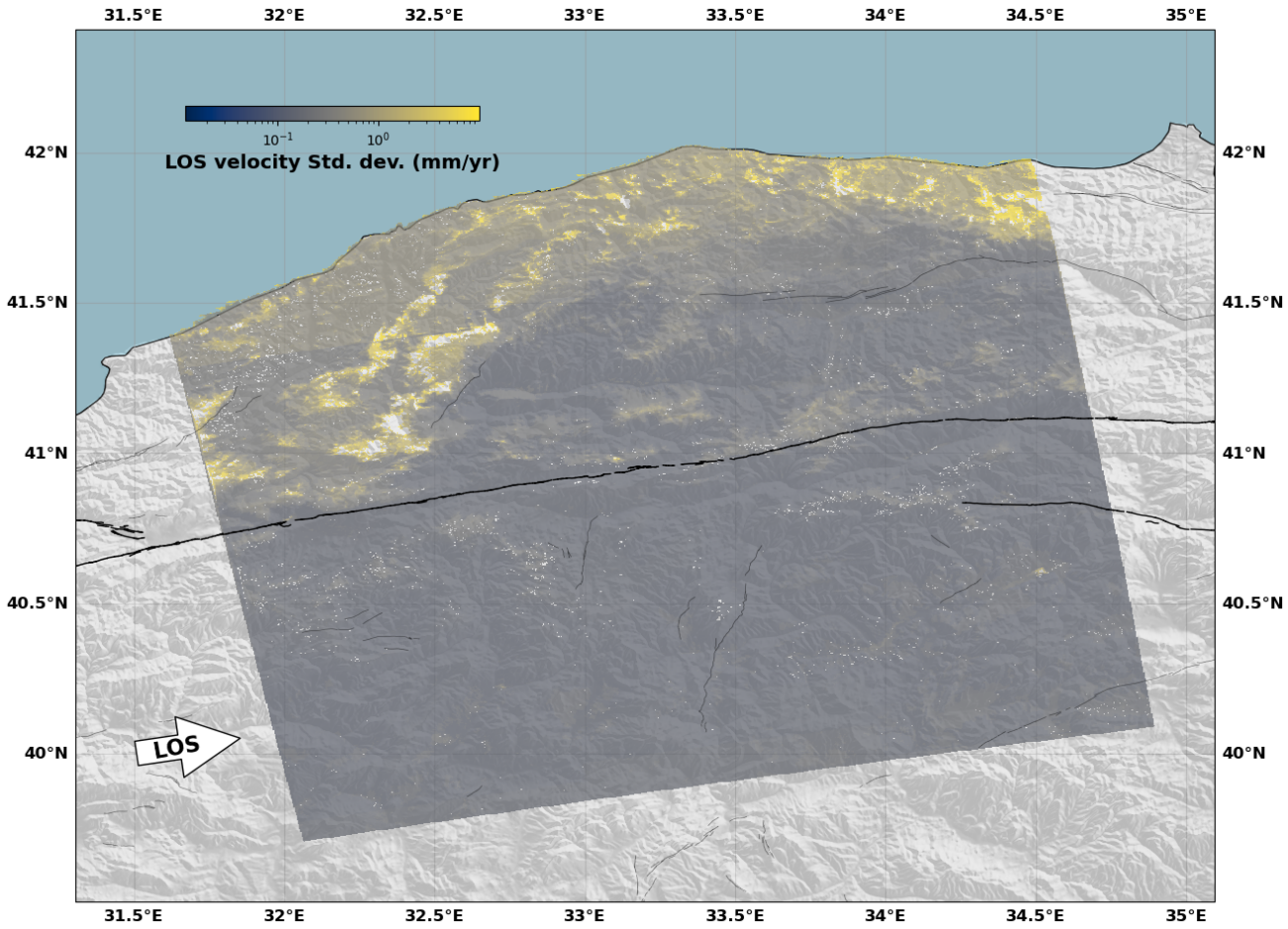

Figure S-8. Line-of-sight velocity standard deviation map from track 87 - Standard deviations are from the analyzed state covariance at the end of the Kalman filtering procedure.

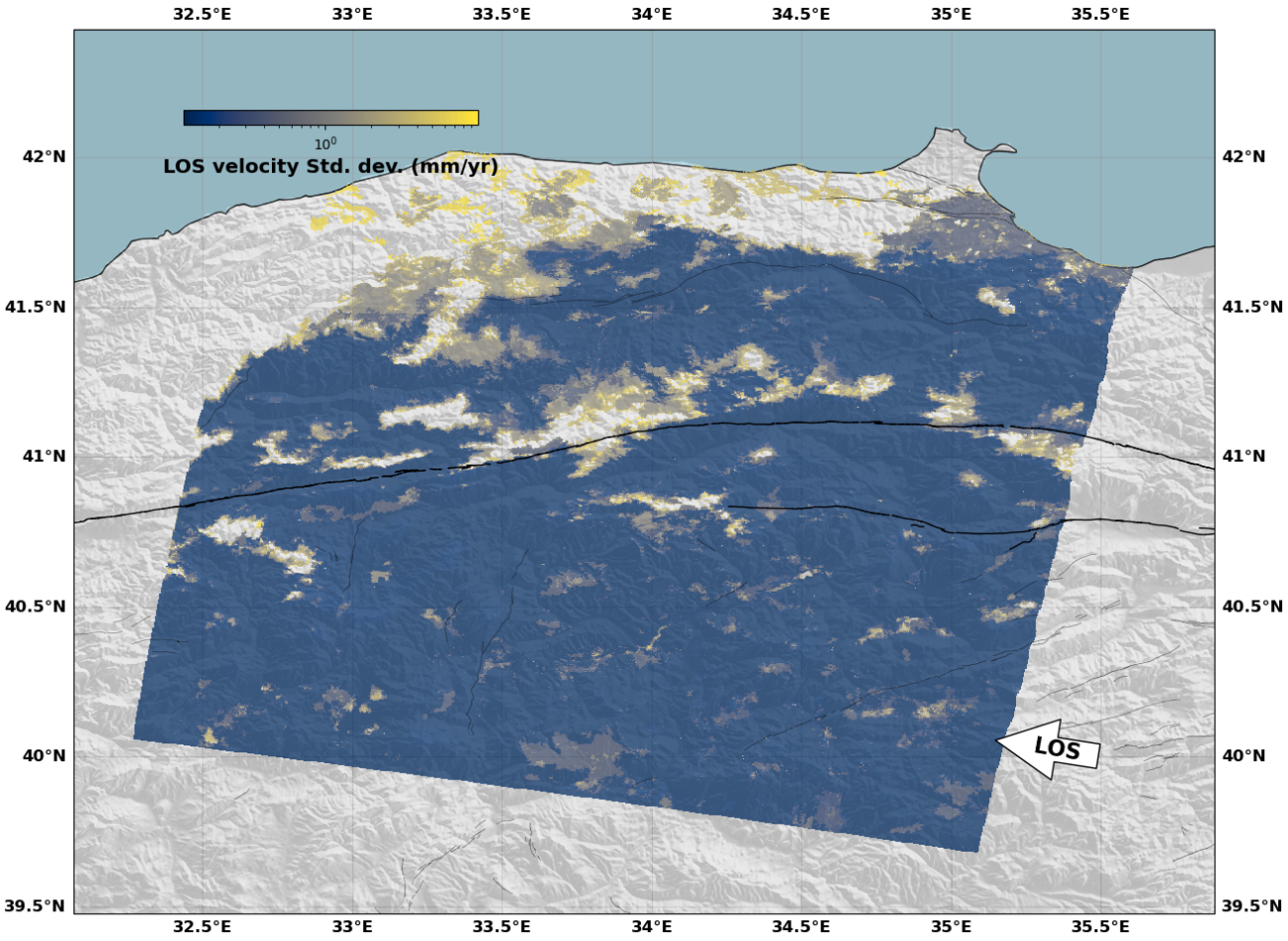

Figure S-9. Line-of-sight velocity map standard deviation from track 167 - Standard deviations are from the analyzed state covariance at the end of the Kalman filtering procedure.

1.4. Number of data per pixel

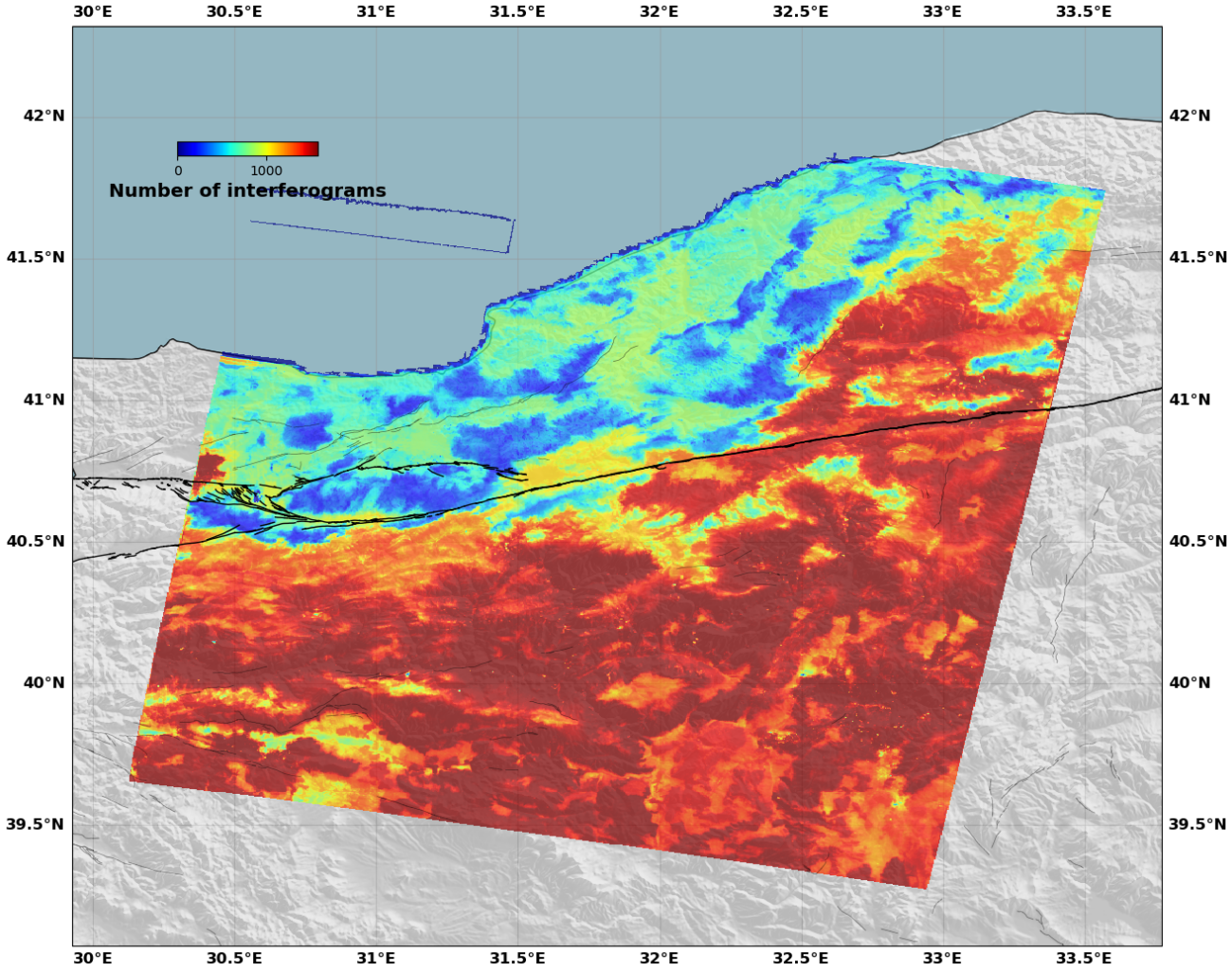

Figure S-10. Number of interferograms available per pixels on track 65 - Map of the number of unwrapped interferograms per pixel, used as one of the quality factor for pixel selection.

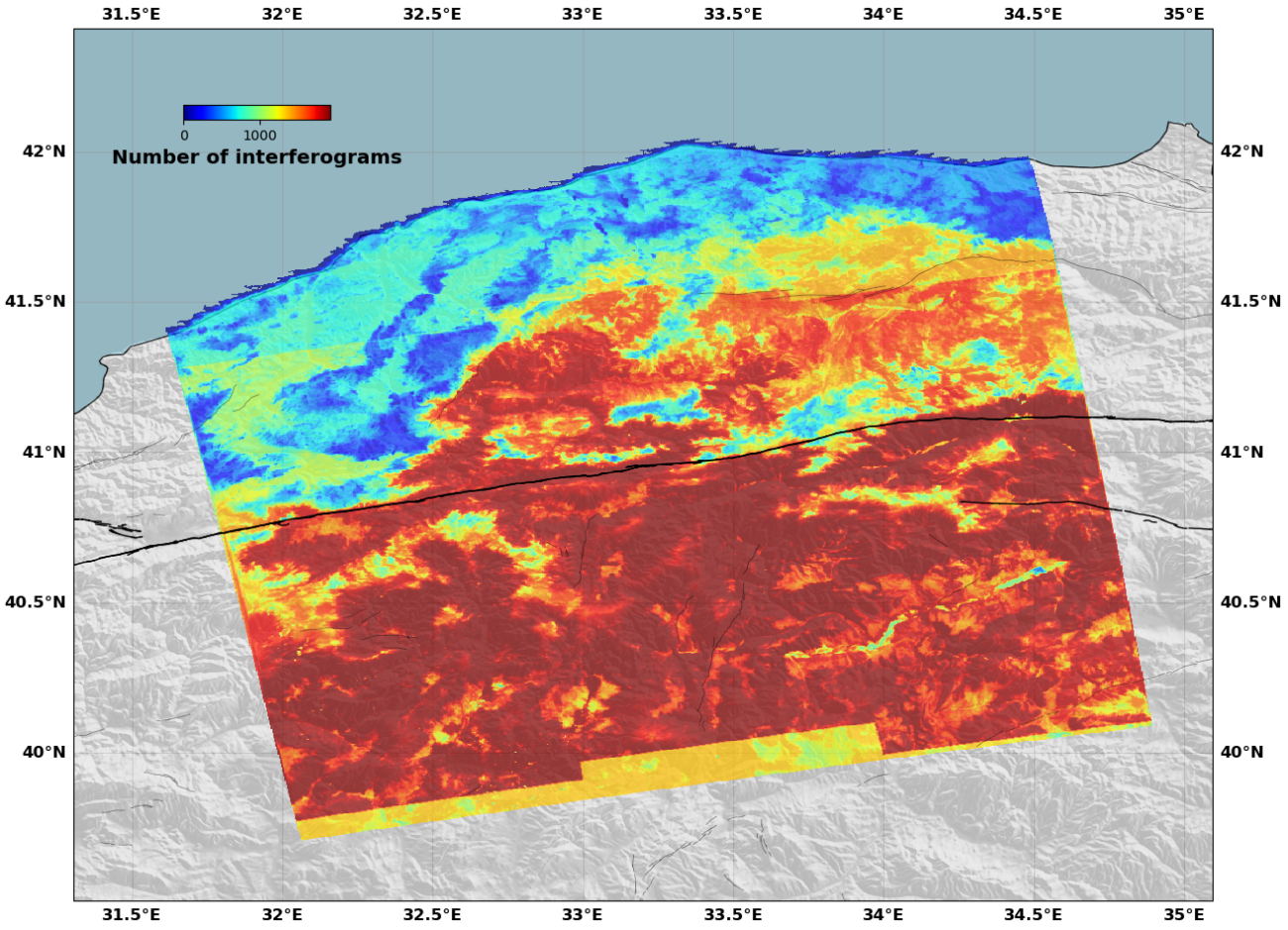

Figure S-11. Number of interferograms available per pixels on track 87 - Map of the number of unwrapped interferograms per pixel, used as one of the quality factor for pixel selection.

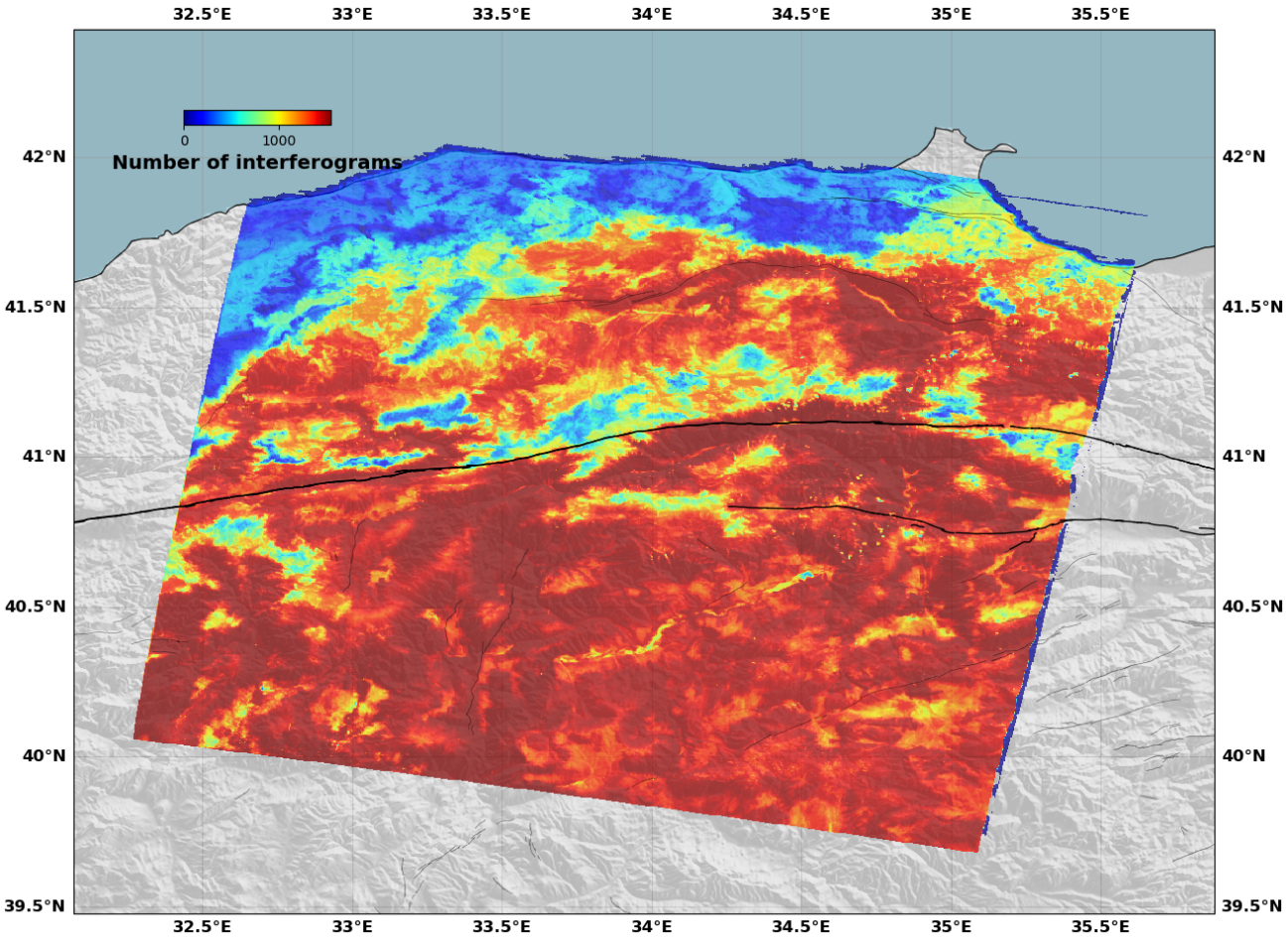

Figure S-12. Number of interferograms available per pixels on 167 - Map of the number of unwrapped interferograms per pixel, used as one of the quality factor for pixel selection.

1.5. RMS of time series reconstruction per pixel

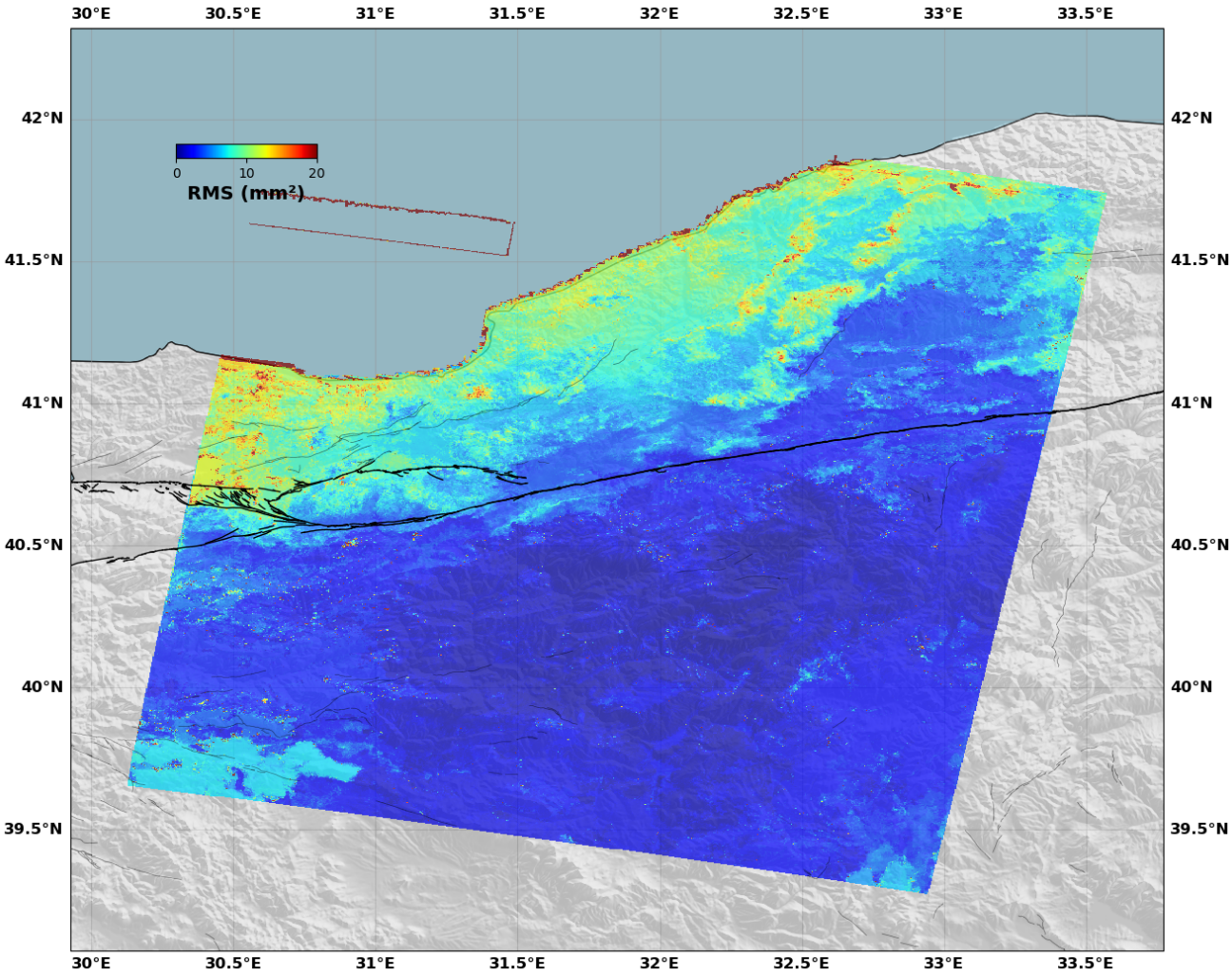

Figure S-13. RMS of time series reconstruction for track 65 - RMS is defined as the average of the square difference between data (i.e. interferograms) and time series reconstructions (i.e. interferograms predicted from the time series) and used as a quality factor for pixel selection.

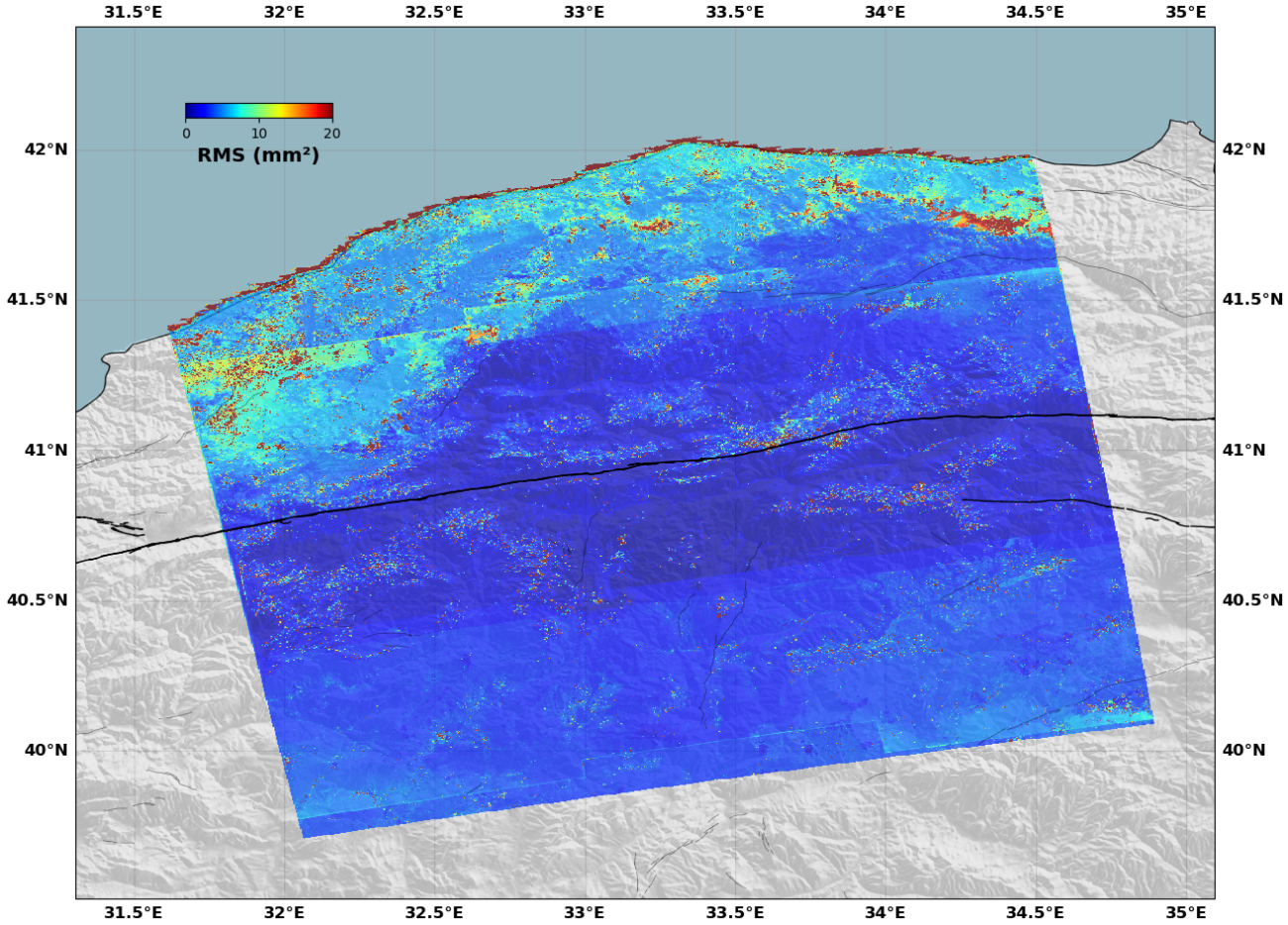

Figure S-14. RMS of time series reconstruction for track 87 - RMS is defined as the average of the square difference between data (i.e. interferograms) and time series reconstructions (i.e. interferograms predicted from the time series) and used as a quality factor for pixel selection.

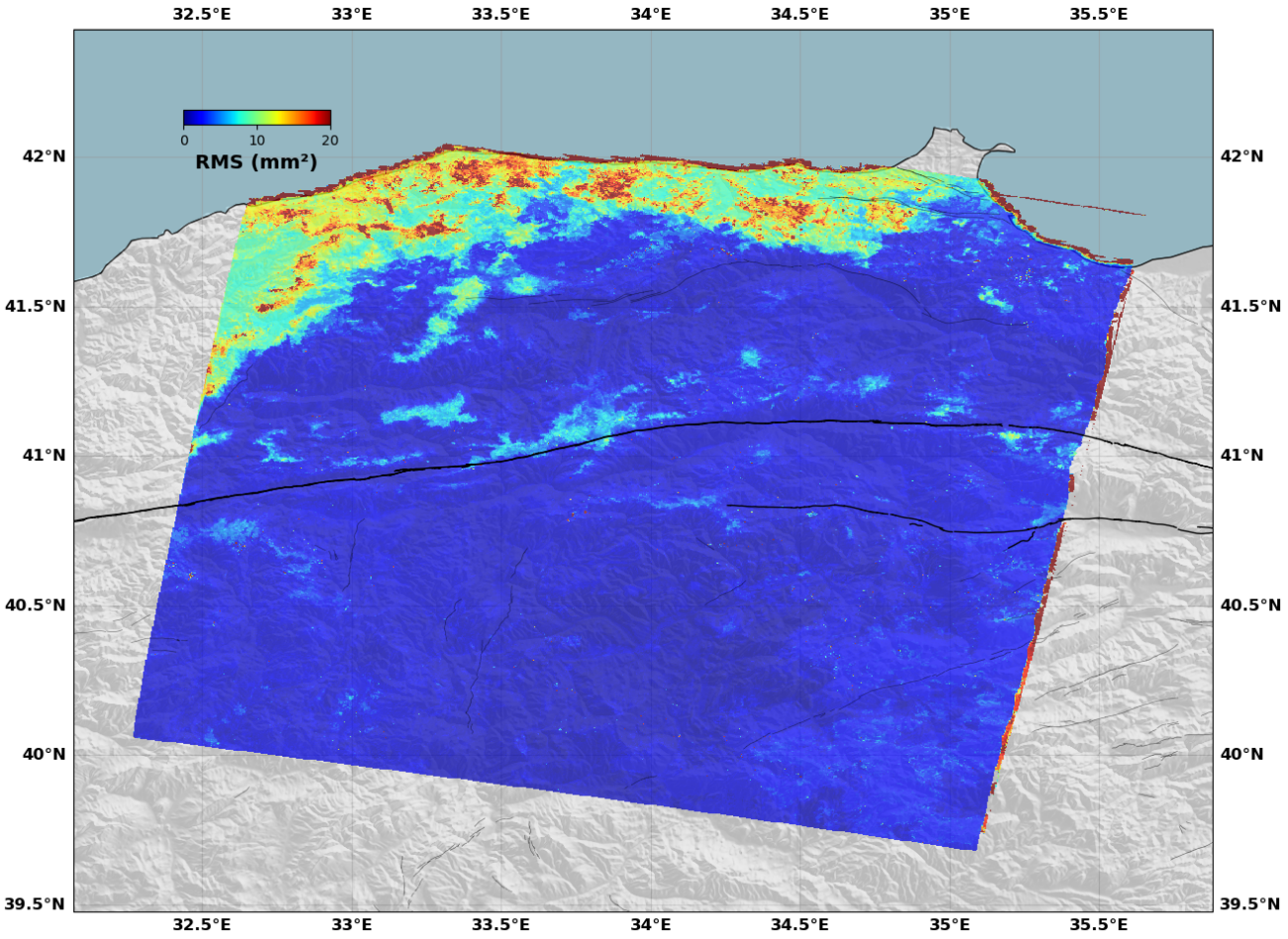

Figure S-15. RMS of time series reconstruction for 167 - RMS is defined as the average of the square difference between data (i.e. interferograms) and time series reconstructions (i.e. interferograms predicted from the time series) and used as a quality factor for pixel selection.

1.6. Additional results

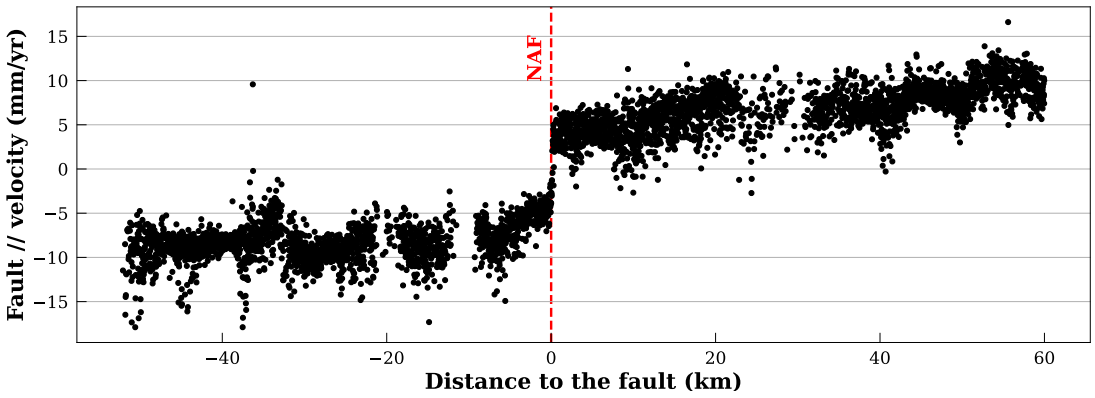

Figure S-16. Fault perpendicular profile of fault parallel ground velocity - This profile intersects the North Anatolian Fault in Ismetpasa.

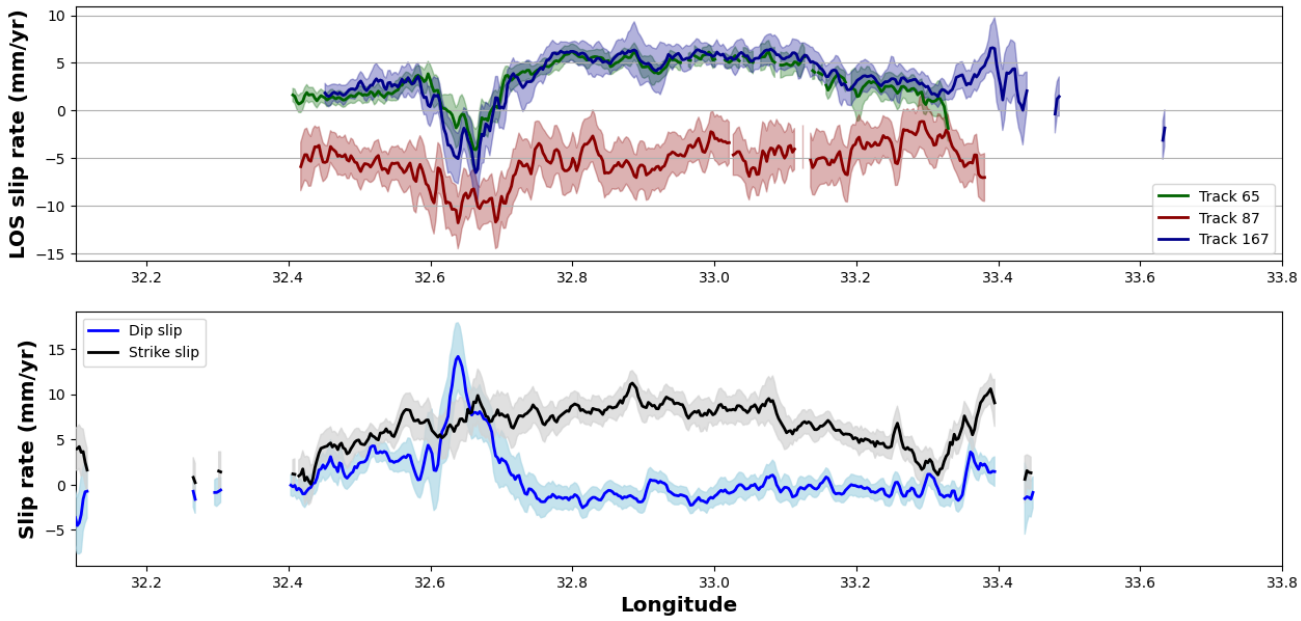

Figure S-17. Along strike distribution of slip - Top Along strike distribution of phase difference across the NAF in LOS for tracks 65 (green), 87 (red) and 167 (blue). Tracks 65 and 167 are both in the same geometry of acquisition (i.e. descending orbit), hence the remarkable agreement between the two independent datasets. Track 87 is along an ascending orbit. When motion is opposite on ascending and descending tracks LOS, ground motion is mostly horizontal as expected motion is aligned with the LOSs. When motion is opposite in LOS, ground motion is mostly vertical. **Bottom** Along strike distribution of horizontal and differential motion from the decomposition of the three tracks. As shown by the agreement between data shown above, ground motion is mostly horizontal (right lateral strike slip) along the fault with some vertical differential motion near Ismetpasa (northern block subsiding wrt. southern block).

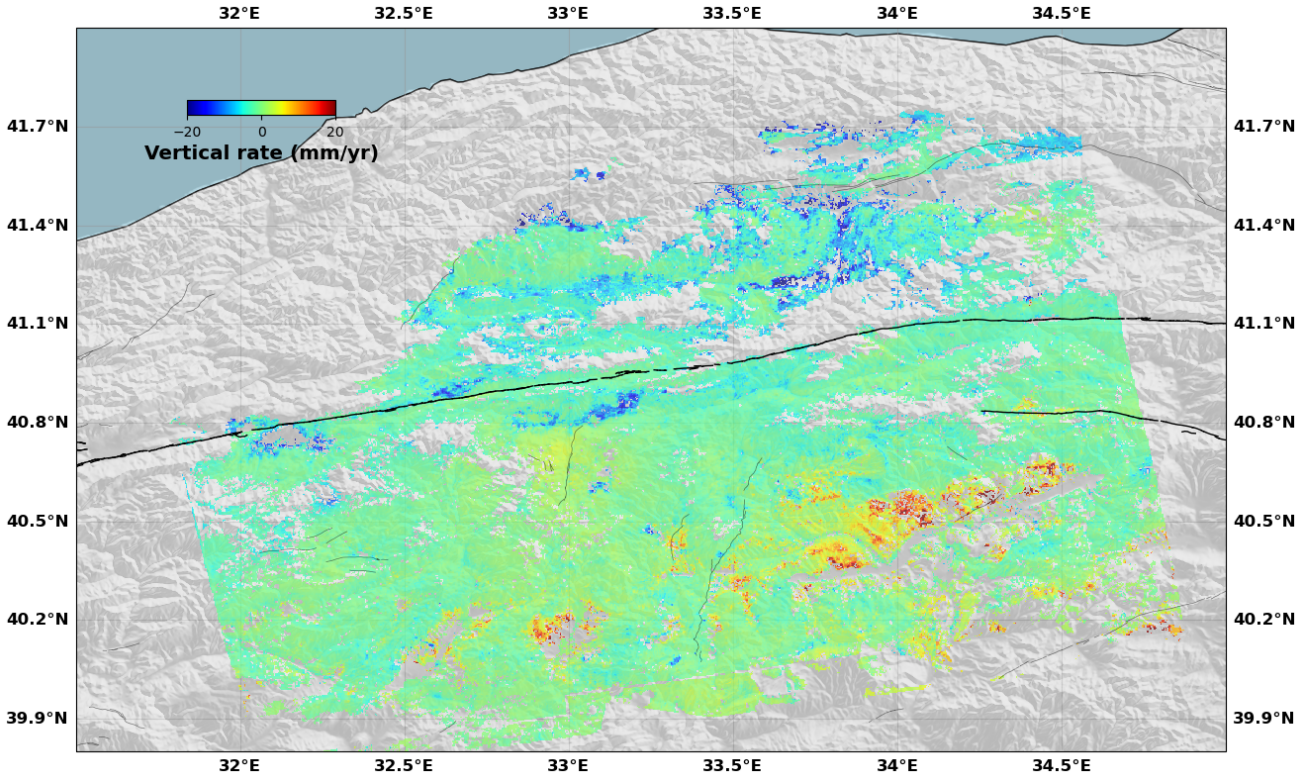

Figure S-18. Map of vertical displacement rate - This map results from the combination of the three velocity maps on track 65, 87 and 167.

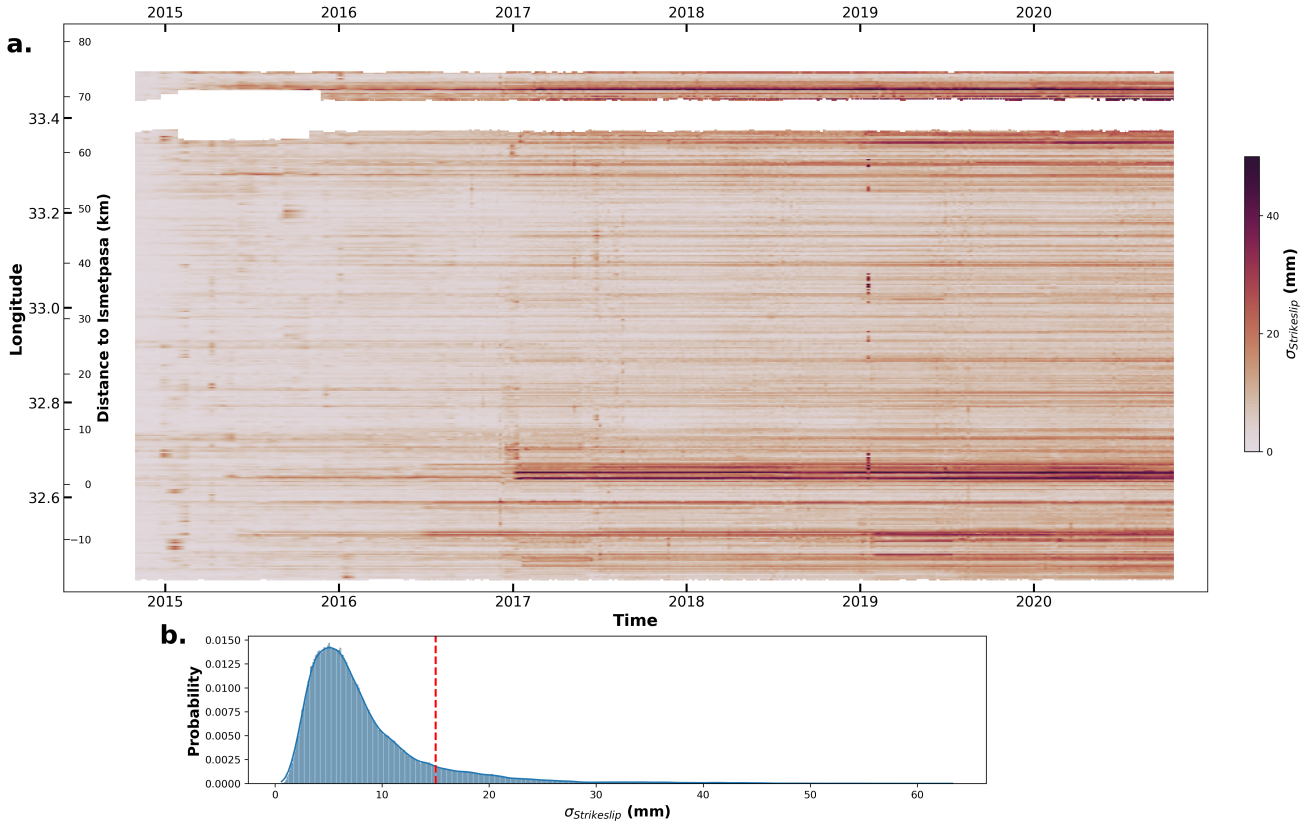

Figure S-19. Uncertainties on strike slip motion - Standard deviation of the strike slip motion as function of time. The uncertainty derives from the general least square inversion of the horizontal vs vertical relative motion between both sides of the fault. We consider the posterior covariance matrix and represent here the square root of the diagonal term. Bottom plot shows the distribution of these uncertainties with the threshold we have chosen for the representation in figure 4 of the main text.

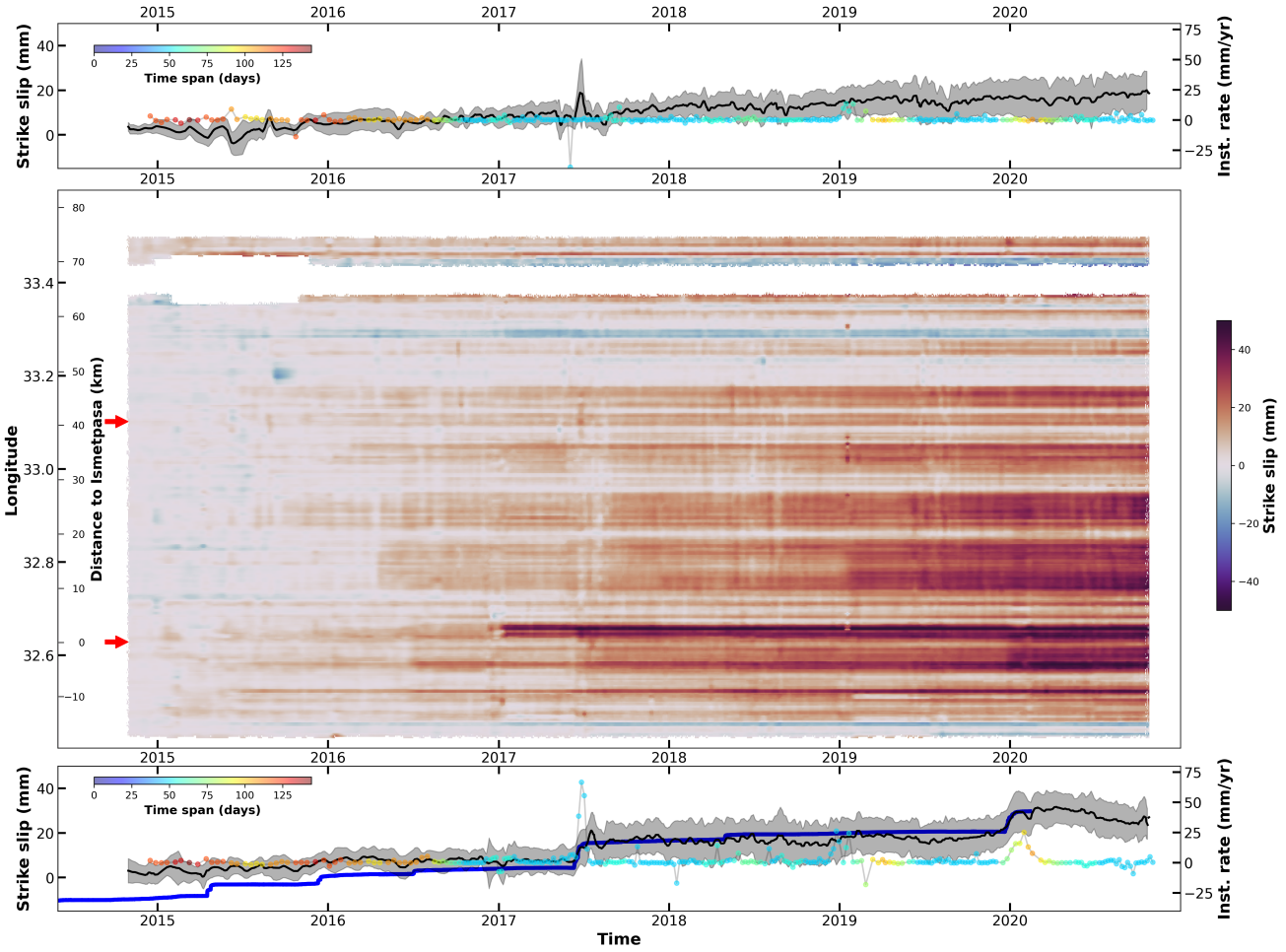

Figure S-20. Time dependent surface slip rate - Same as figure 4 of the main text without masking uncertain values.

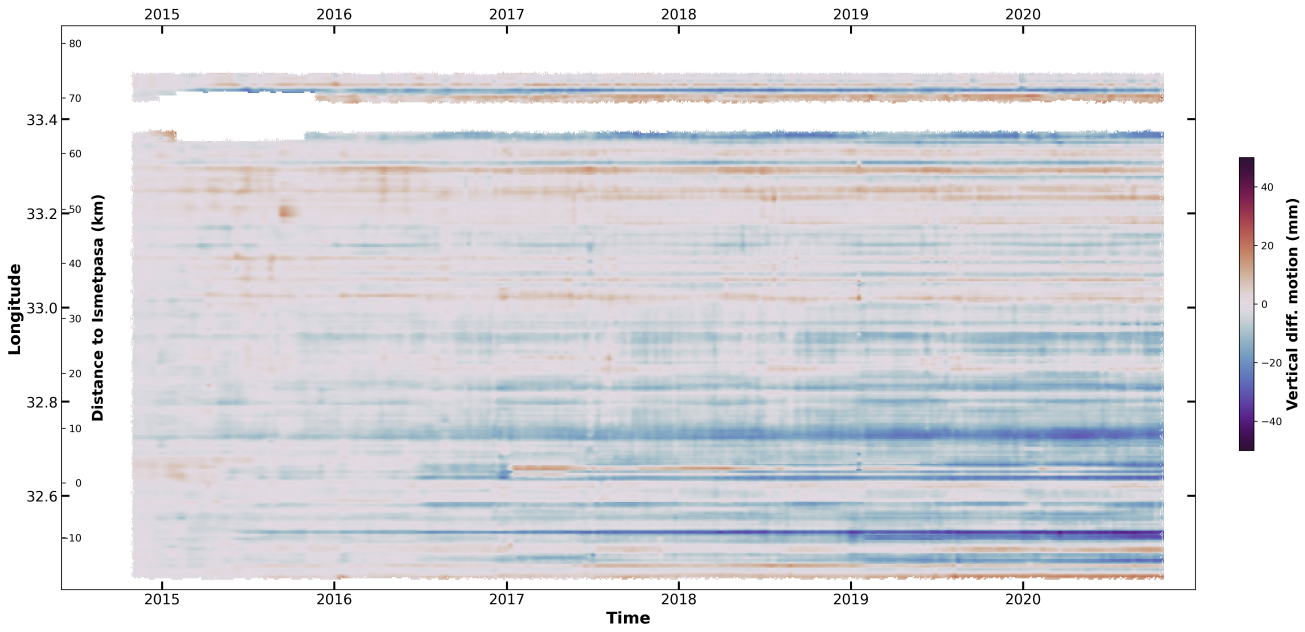

Figure S-21. Time-dependent vertical differential motion - Evolution of the vertical differential motion across the NAF. Blue indicates subsidence of the northern block wrt. the south.

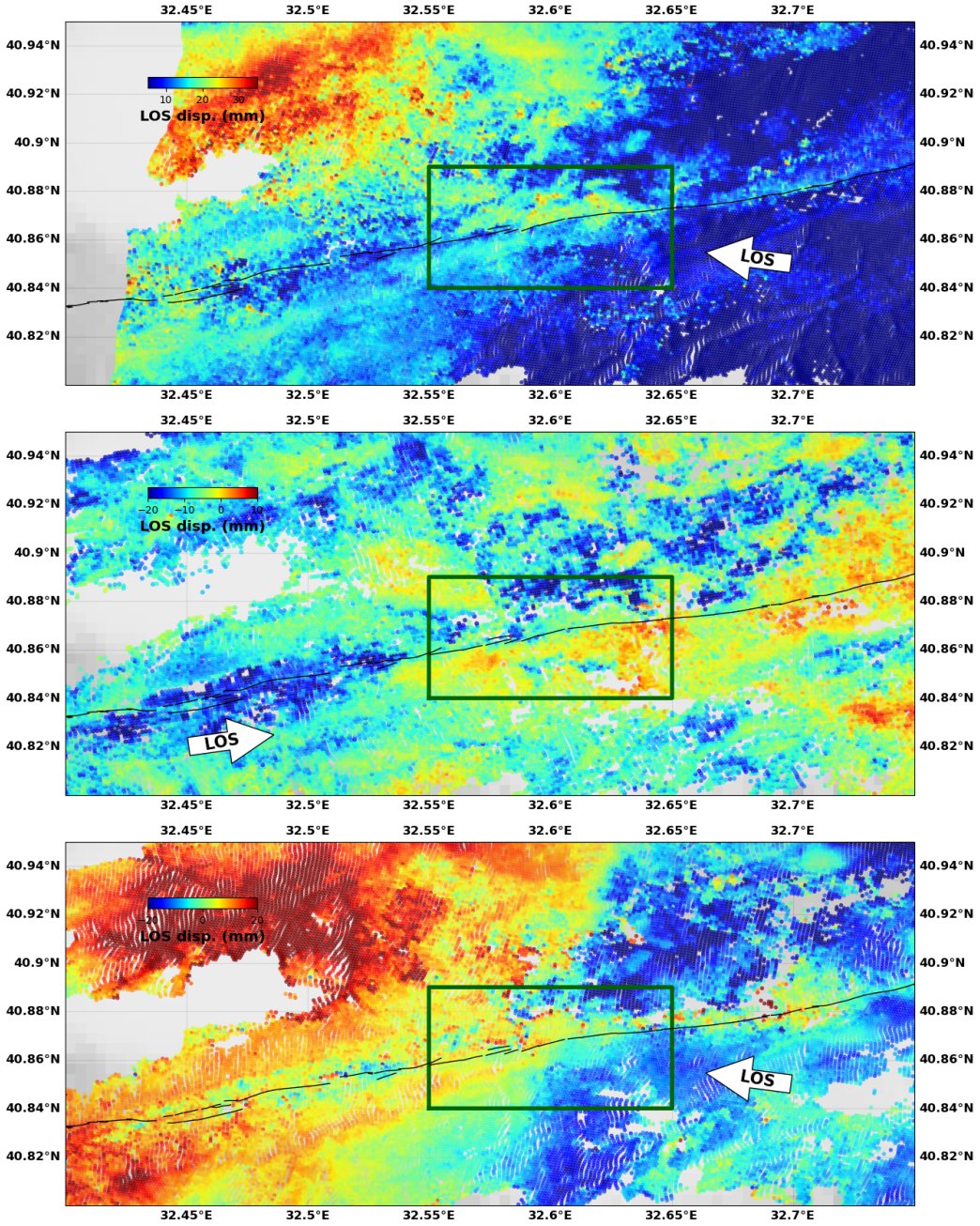

Figure S-22. LOS displacement resulting from the slow slip event of 2017 - Difference between time frames of the time series bracketing the slow slip event of 2017 from data on tracks 167 (top), 87 (center) and 65 (bottom). The white arrow indicates the direction from the satellite to the ground. Dark lines are fault traces. Dark rectangle indicates the region where the slow slip event is identified. The opposite sign of the across fault gradient between data on ascending and descending tracks confirms that motion is mainly horizontal.

2. GNSS dataset

We processed data from 77 continuous GNSS located in Eurasian (48 stations), Anatolian (21 stations), African (5 stations), Arabian (2 plates) and Somalia (1 station) Plates (Figure 1, a and b). We provide in table S-1 and S-2 the observation periods used in this paper and the measured velocities in the ITRF Eurasia-fixed reference frame, with our model predictions. Sites are grouped within the following networks:

• 8 GNSS from the International GNSS service, core network (`www.igs.org`): BHR4, CHUM, KIT3, MAT1, MDVJ, ONS1, POL2, RAMO, TASH

• 29 GNSS from the International GNSS service (`www.igs.org`): ADIS, ANKR, ARUC, BSHM, BUCU, CRAO, DJIG, DRAG, DYNG, GANP, GLSV, GRAZ, ISBA, ISTA, IZMI, KITG, KRS1, MERS, MIKL, NICO, ORID, PENC, POLV, SOFI, SULP, TEHN, TUBI, WARN, ZECK.

• 20 GNSS from the Turkish National Network (`https://www.tusaga-aktif.gov.tr/`): BOLU, BOL1, BOYT, CANK, CMLD, CORU, ESKS, HEND, HYMN, INE2, KKAL, KRBK, KSTM, KURU, NAHA, SIH1, SINP, SUNL, VEZI, ZONG.

• 19 GNSS from the ISMENET network: IS01, IS02, IS03, IS04, IS05, IS07, IS08, IS09, IS10, IS11, IS12, IS13, IS14, IS16, IS17, IS18, IS19, IS20, IS21. Each station of Ismenet includes a Zephyr geodetic antenna bolted in a boulder or custom made concrete monument and a NetR9 or NetRS receiver (Trimble) recording at 30 seconds, powered by either local power or solar panels. Antennas are covered by a radome.

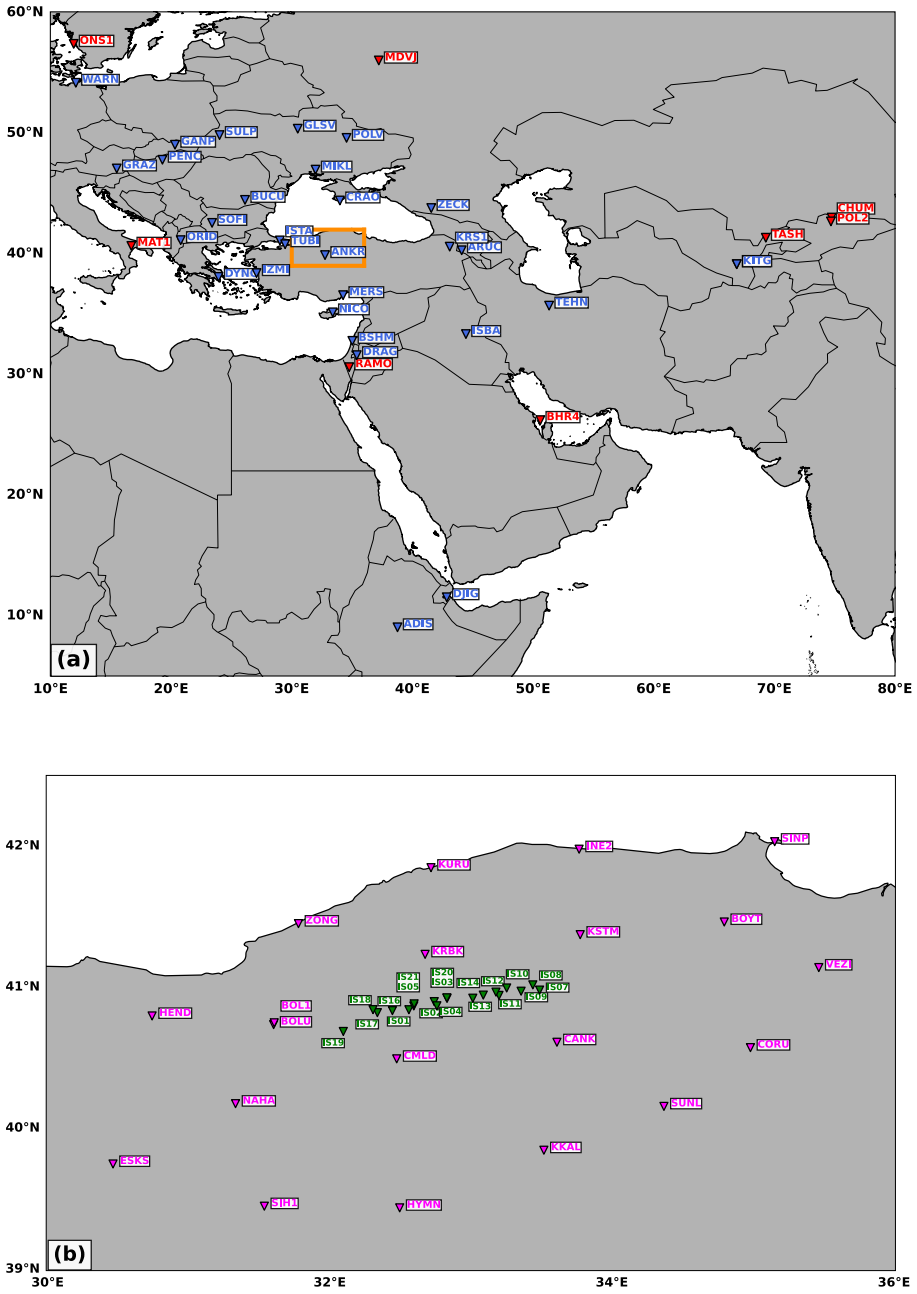

Figure S-23. Selection of GNSS sites - a. Extended selection including IGS, core network, sites (red) and IGS stations (blue). **b.** Local selection with sites from the Turkish Nation Network (pink) and from our ISMENET network (green).

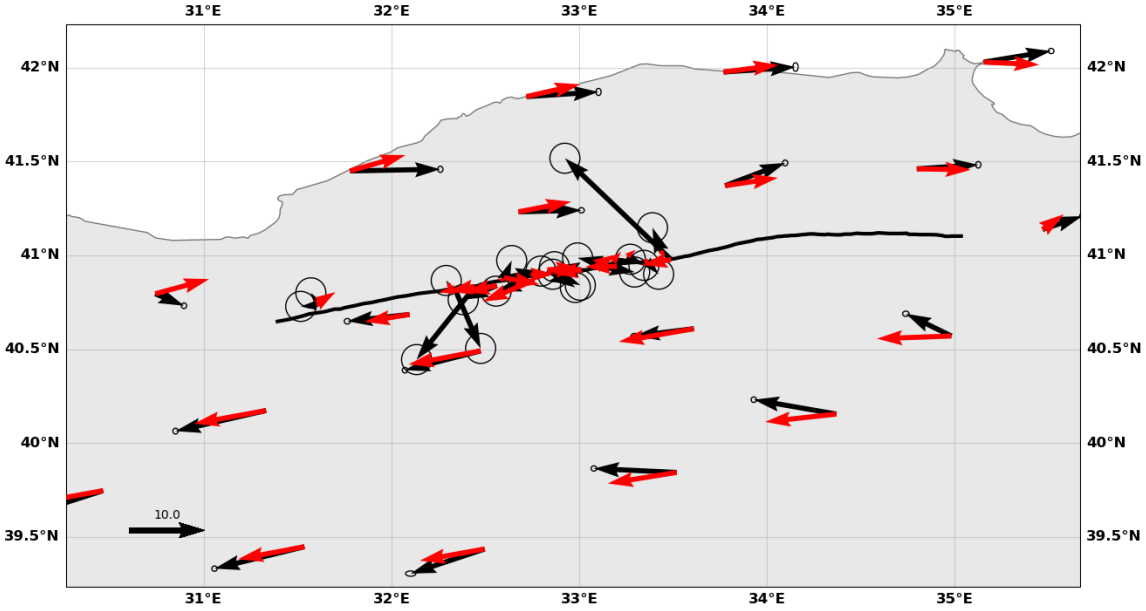

Figure S-24. GNSS derived velocities and predictions from the mean model - Map of the GNSS-derived velocities (black) together with the predictions from the mean model. Ellipses are 1-sigma. It is important to note that the mean model is not a model drawn from the posterior PDF, hence its predictions are not necessarily the best ones. In addition, error ellipses here only represent the formal uncertainties on the GNSS measurements feeding in $\mathbf{C}_d$ while our Bayesian approach assumes larger uncertainties deriving from the prediction error, $\mathbf{C}_p$.

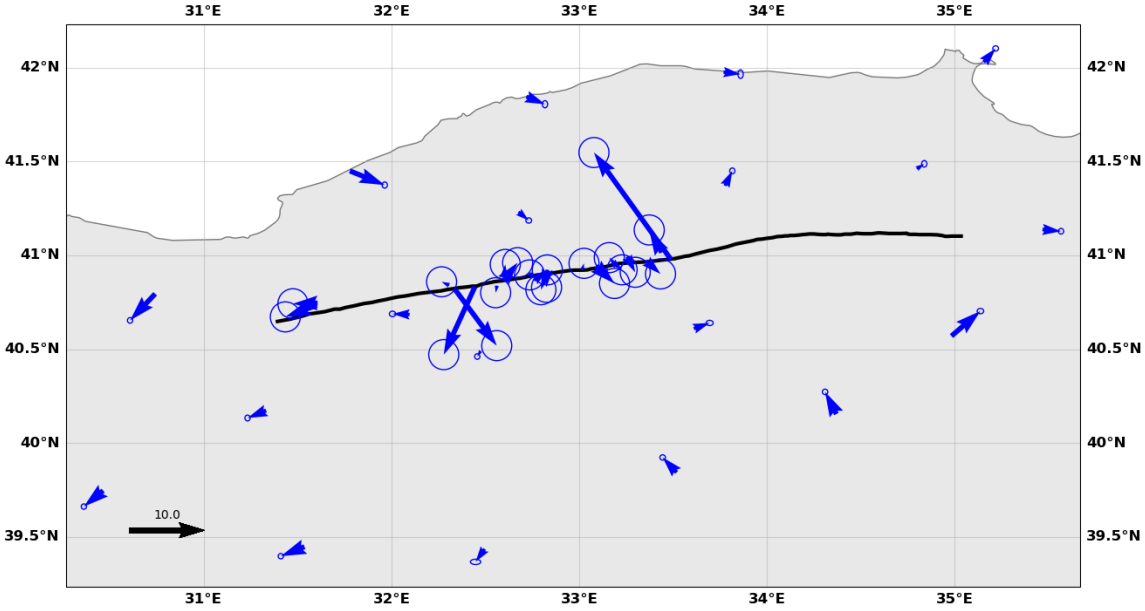

Figure S-25. Residuals from the mean model - Map of the residuals, as differences between velocities (black arrows on figure S-24) and predictions from the mean model (red arrows on figure S-24). Ellipses are 1-sigma. It is important to note that the mean model is not a model drawn from the posterior PDF, hence its predictions are not necessarily the best ones. In addition, error ellipses here only represent the formal uncertainties on the GNSS measurements feeding in $\mathbf{C}_d$ while our Bayesian approach assumes larger uncertainties deriving from the prediction error, $\mathbf{C}_p$.

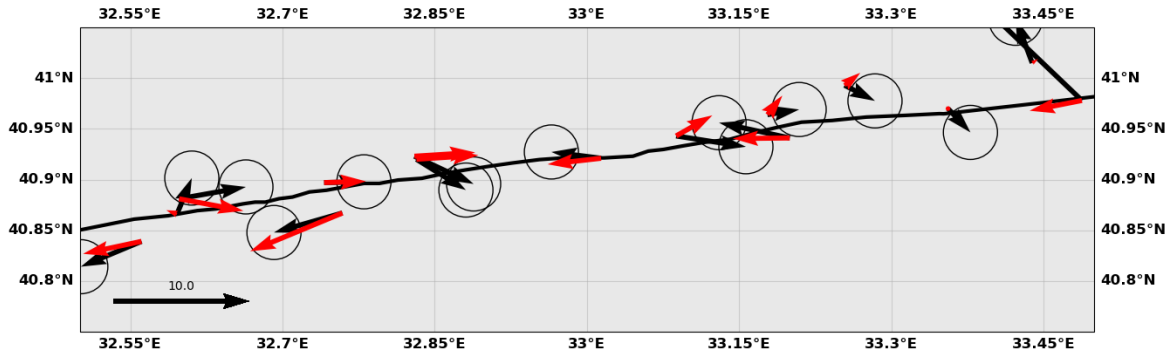

Figure S-26. GNSS derived velocities and predictions from the mean model (close up) - Map of the GNSS-derived velocities (black) together with the predictions from the mean model. Ellipses are 1-sigma. It is important to note that the mean model is not a model drawn from the posterior PDF, hence its predictions are not necessarily the best ones. In addition, error ellipses here only represent the formal uncertainties on the GNSS measurements feeding in $\mathbf{C}_d$ while our Bayesian approach assumes larger uncertainties deriving from the prediction error, $\mathbf{C}_p$.

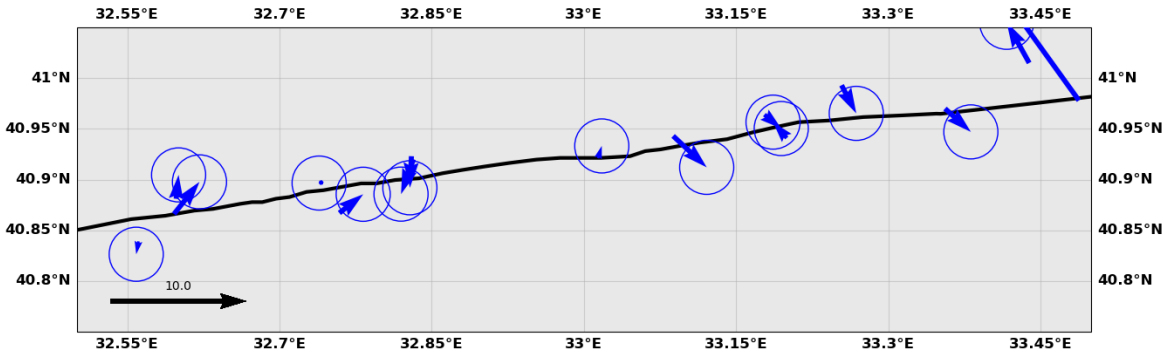

Figure S-27. Residuals from the mean model (close up)- Map of the residuals, as differences between velocities (black arrows on figure S-24) and predictions from the mean model (red arrows on figure S-24). Ellipses are 1-sigma. It is important to note that the mean model is not a model drawn from the posterior PDF, hence its predictions are not necessarily the best ones. In addition, error ellipses here only represent the formal uncertainties on the GNSS measurements feeding in $\mathbf{C}_d$ while our Bayesian approach assumes larger uncertainties deriving from the prediction error, $\mathbf{C}_p$.

NAME	Lon (^{o})	Lat (^{o})	First Obs (dec year)	Last Obs (dec year)
BOL1	31.606	40.746	2018.884	2021.578
BOLU	31.602	40.734	2016.534	2018.774
BOYT	34.797	41.461	2016.534	2021.578
CANK	33.610	40.609	2016.534	2021.578
CMLD	32.475	40.491	2016.534	2021.578
CORU	34.982	40.570	2016.534	2021.578
ESKS	30.464	39.746	2016.534	2021.578
HEND	30.741	40.795	2016.534	2021.578
HYMN	32.496	39.435	2016.534	2020.750
INE2	33.768	41.977	2016.534	2020.127
KKAL	33.518	39.843	2016.534	2021.578
KRBK	32.676	41.232	2016.534	2021.578
KSTM	33.776	41.371	2016.534	2021.578
KURU	32.718	41.846	2016.534	2021.578
NAHA	31.332	40.173	2016.534	2021.578
SIH1	31.536	39.447	2016.534	2021.578
SINP	35.154	42.030	2016.534	2021.578
SUNL	34.369	40.154	2016.534	2020.059
VEZI	35.467	41.138	2016.534	2021.578
ZONG	31.778	41.450	2016.534	2021.578
IS01	32.561	40.839	2016.537	2021.578
IS02	32.741	40.897	2016.534	2021.578
IS03	32.832	40.920	2016.534	2019.453
IS04	32.759	40.867	2016.542	2021.578
IS05	32.596	40.866	2016.944	2019.448
IS07	33.488	40.978	2019.456	2021.578
IS08	33.439	41.015	2019.456	2021.578
IS09	33.356	40.970	2019.456	2021.578
IS10	33.254	40.993	2019.456	2021.578
IS11	33.200	40.941	2019.440	2021.578

IS12	33.178	40.964	2019.440	2021.578
IS13	33.088	40.943	2019.462	2021.578
IS14	33.014	40.921	2019.442	2021.578
IS16	32.444	40.833	2019.451	2021.578
IS17	32.338	40.818	2019.451	2021.578
IS18	32.307	40.840	2019.445	2021.578
IS19	32.096	40.685	2019.445	2021.578
IS20	32.830	40.923	2019.456	2021.578
IS21	32.598	40.881	2019.451	2021.578

Table S-1: **GNSS observation period -** Period of observation for the stations used in this study. Sites with names starting with IS have been installed over the duration of the Geo4D project.

Site	**Lon**	**Lat**	**Data**		**Ref. removed**		**Model**	
			East	North	East	North	East	North
	(°E)	(°N)	(mm/yr)		(mm/yr)		(mm/yr)	
BOL1	31.606	40.746	-11.288	1.658	-0.812	1.364	2.333	1.425
BOLU	31.602	40.734	-12.533	0.150	-2.058	-0.144	2.032	1.375
BOYT	34.797	41.461	-2.306	1.212	8.235	0.699	6.768	-0.107
CANK	33.610	40.609	-18.258	-0.437	-7.795	-0.869	-9.410	-1.626
CMLD	32.475	40.491	-20.448	-2.175	-9.996	-2.529	-9.063	-1.735
CORU	34.982	40.570	-16.440	3.662	-5.979	3.135	-9.325	-0.321
ESKS	30.464	39.746	-22.154	-3.658	-11.767	-3.871	-8.779	-1.599
HEND	30.741	40.795	-6.565	-1.383	3.917	-1.617	6.812	1.830
HYMN	32.496	39.435	-20.045	-2.878	-9.689	-3.233	-8.104	-1.467
INE2	33.768	41.977	-0.994	1.224	9.593	0.782	6.868	0.897
KKAL	33.518	39.843	-21.268	1.046	-10.875	0.620	-8.596	-1.381
KRBK	32.676	41.232	-2.085	0.631	8.434	0.263	6.625	1.256
KSTM	33.776	41.371	-2.482	3.587	8.050	3.144	6.638	0.991

KURU	32.718	41.846	-0.953	1.058	9.622	0.687	6.695	1.539
NAHA	31.332	40.173	-22.371	-2.478	-11.947	-2.752	-9.020	-1.634
SIH1	31.536	39.447	-22.170	-2.629	-11.812	-2.916	-8.289	-1.555
SINP	35.154	42.030	-1.619	2.183	8.974	1.647	6.933	-0.319
SUNL	34.369	40.154	-21.295	2.540	-10.873	2.055	-8.906	-0.973
VEZI	35.467	41.138	-5.164	2.521	5.349	1.962	2.693	1.947
ZONG	31.778	41.450	1.545	0.546	12.085	0.239	6.955	1.976
IS01	32.561	40.839	-14.892	-1.461	-4.408	-1.821	-4.220	-0.934
IS02	32.741	40.897	-7.470	0.490	3.019	0.118	3.148	0.093
IS03	32.832	40.920	-6.757	-1.834	3.734	-2.213	4.631	0.287
IS04	32.759	40.867	-15.465	-1.008	-4.979	-1.382	-6.709	-2.817
IS05	32.596	40.866	-9.314	3.076	1.172	2.714	-0.715	0.274
IS07	33.488	40.978	-24.545	14.010	-14.049	13.586	-3.717	-0.733
IS08	33.439	41.015	-11.663	3.820	-1.163	3.400	0.474	0.301
IS09	33.356	40.970	-8.766	-1.259	1.729	-1.674	-0.133	-0.016
IS10	33.254	40.993	-8.176	-0.664	2.322	-1.072	1.187	0.932
IS11	33.200	40.941	-15.648	1.616	-5.155	1.212	-4.080	-0.014
IS12	33.178	40.964	-8.079	0.865	2.416	0.463	1.159	1.418
IS13	33.088	40.943	-5.261	-0.326	5.232	-0.722	2.739	1.534
IS14	33.014	40.921	-14.088	0.928	-3.597	0.537	-3.850	-0.429
IS16	32.444	40.833	-18.174	-9.313	-7.691	-9.665	-3.527	-0.675
IS17	32.338	40.818	-6.993	-7.463	3.489	-7.807	-2.052	-0.390
IS18	32.307	40.840	-10.802	1.037	-0.318	0.695	0.673	0.148
IS19	32.096	40.685	-18.671	-0.552	-8.201	-0.880	-5.683	-0.940
IS20	32.830	40.923	-6.038	-1.609	4.453	-1.987	4.545	0.266
IS21	32.598	40.881	-5.467	1.295	5.020	0.933	4.823	-0.910

Table S-2: **GNSS data, corrected data and model -** Table of GNSS rates used in this article. Data refers to the original GNSS velocities in the Eurasia-fixed referenced frame. Ref. removed refers to the original velocities corrected from the translation and rotation term inferred in the inversion procedure. Model refers to the displacement rates predicted by the slip model. Sites with names starting with IS have been installed over the duration of the Geo4D project.

3. Model additional information and performance

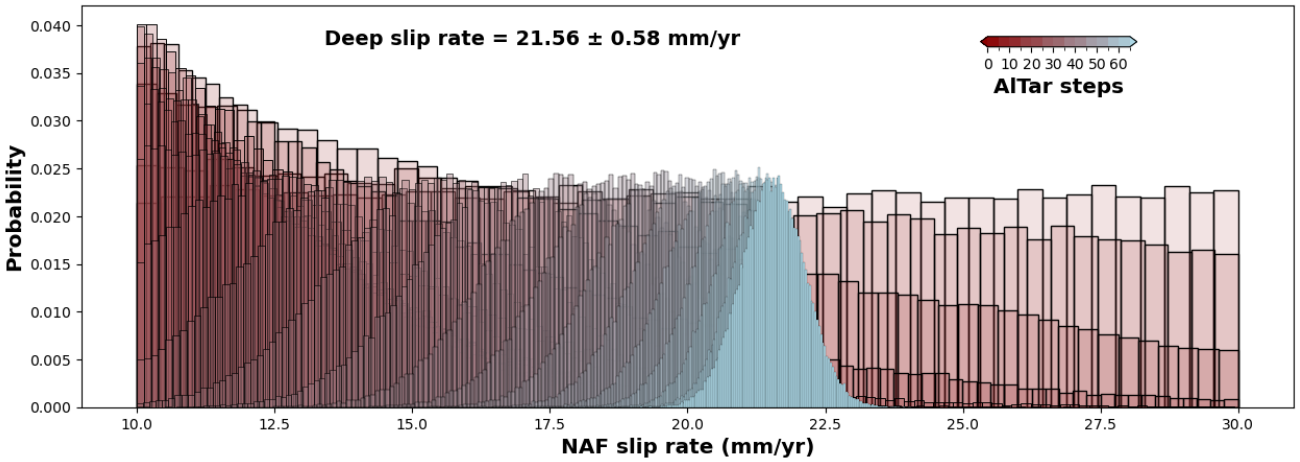

Figure S-28. Example of convergence during tempering - While the sampler marches forward, it progressively shrinks the sample set onto the final, posterior PDF. Here, we show the marginal PDF of the deep slip rate on the NAF, which transitions at each step from the a priori uniform distribution to the posterior, which, in this case, is a Gaussian distribution.

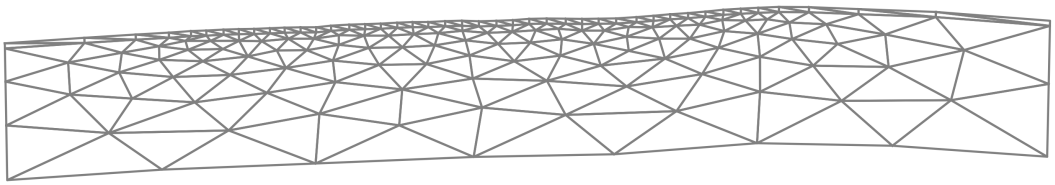

Figure S-29. Triangular mesh for the shallow part of the NAF - 3D representation of the triangular mesh used for the shallow section of the NAF. Shallowest triangles are 1 km-sized while largest, deepest ones are 10 km-size. Shallowest row intersects the surface while deepest row reaches 20 km.

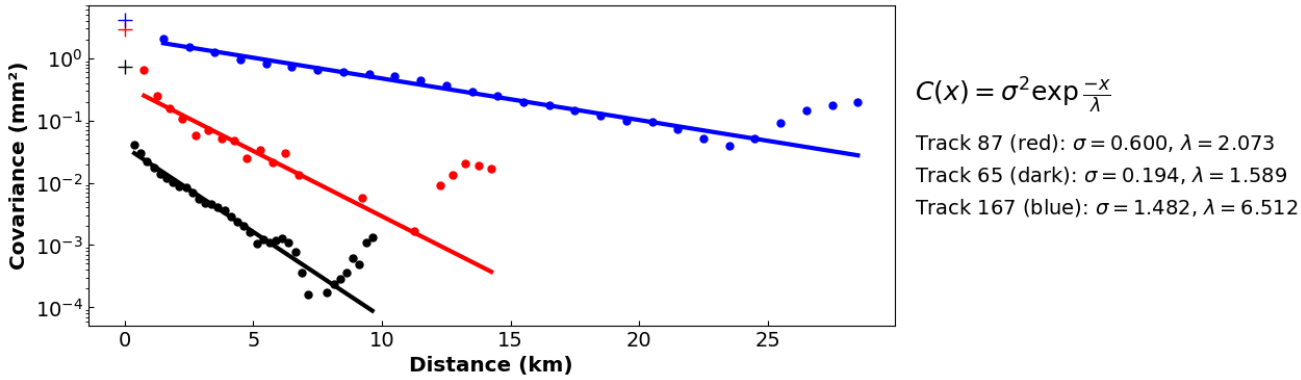

Figure S-30. Covariance functions for the InSAR velocity maps - Empirical covariances of the velocity maps from tracks 65 (dark), 87 (red) and 167 (red). Dots are the empirical covariances. Lines are the exponential fit to the covariance functions. Crosses are the variance of the data (auto-correlation).

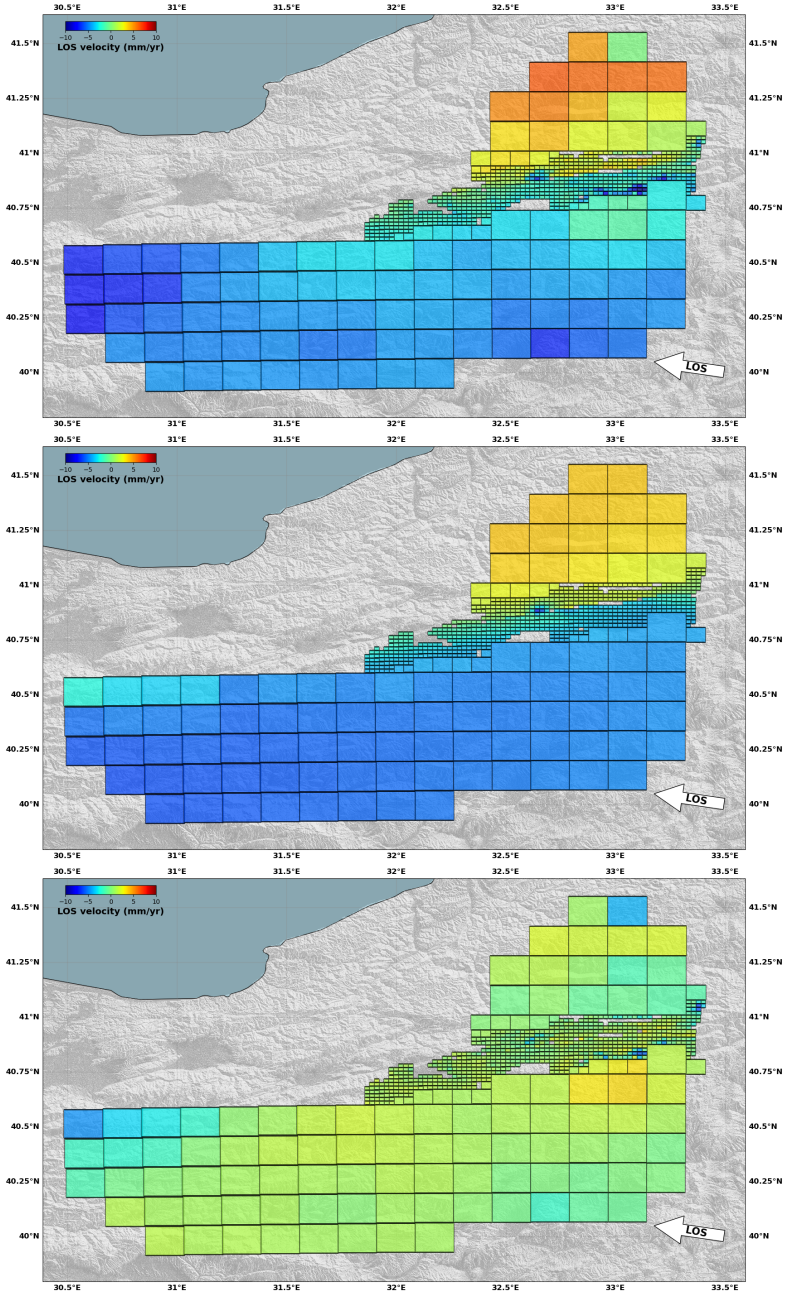

Figure S-31. Decimated velocity field from track 65 - Decimation geometry and resulting input data set for the slip rate inversion (top), prediction from the mean model (center) and residuals (bottom).

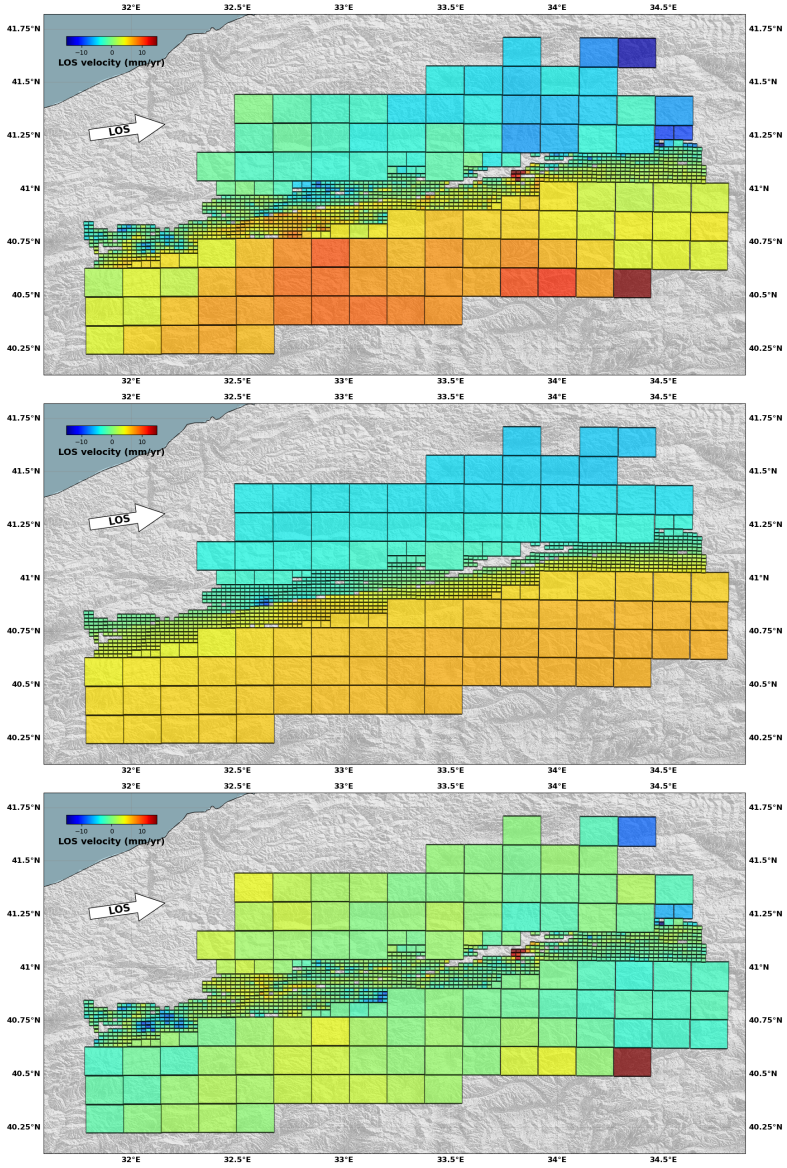

Figure S-32. Decimated velocity field from track 87 - Decimation geometry and resulting input data set for the slip rate inversion (top), prediction from the mean model (center) and residuals (bottom).

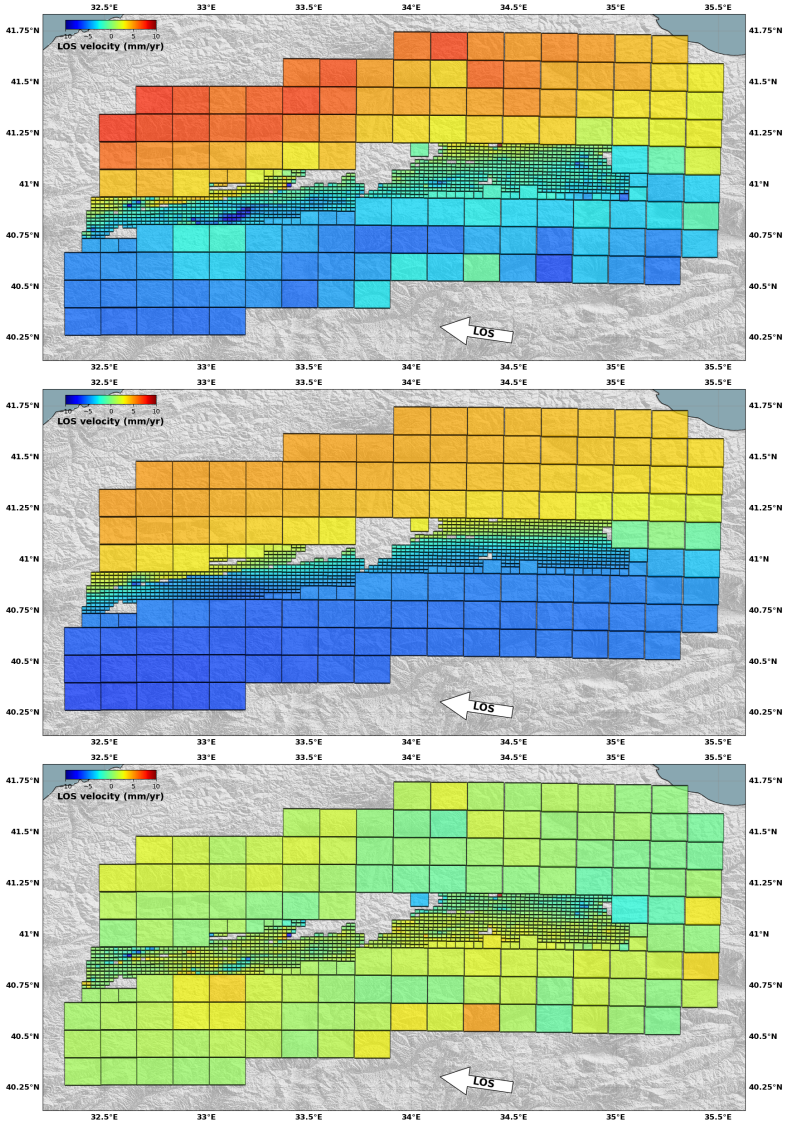

Figure S-33. Decimated velocity field from track 167 - Decimation geometry and resulting input data set for the slip rate inversion (top), prediction from the mean model (center) and residuals (bottom).

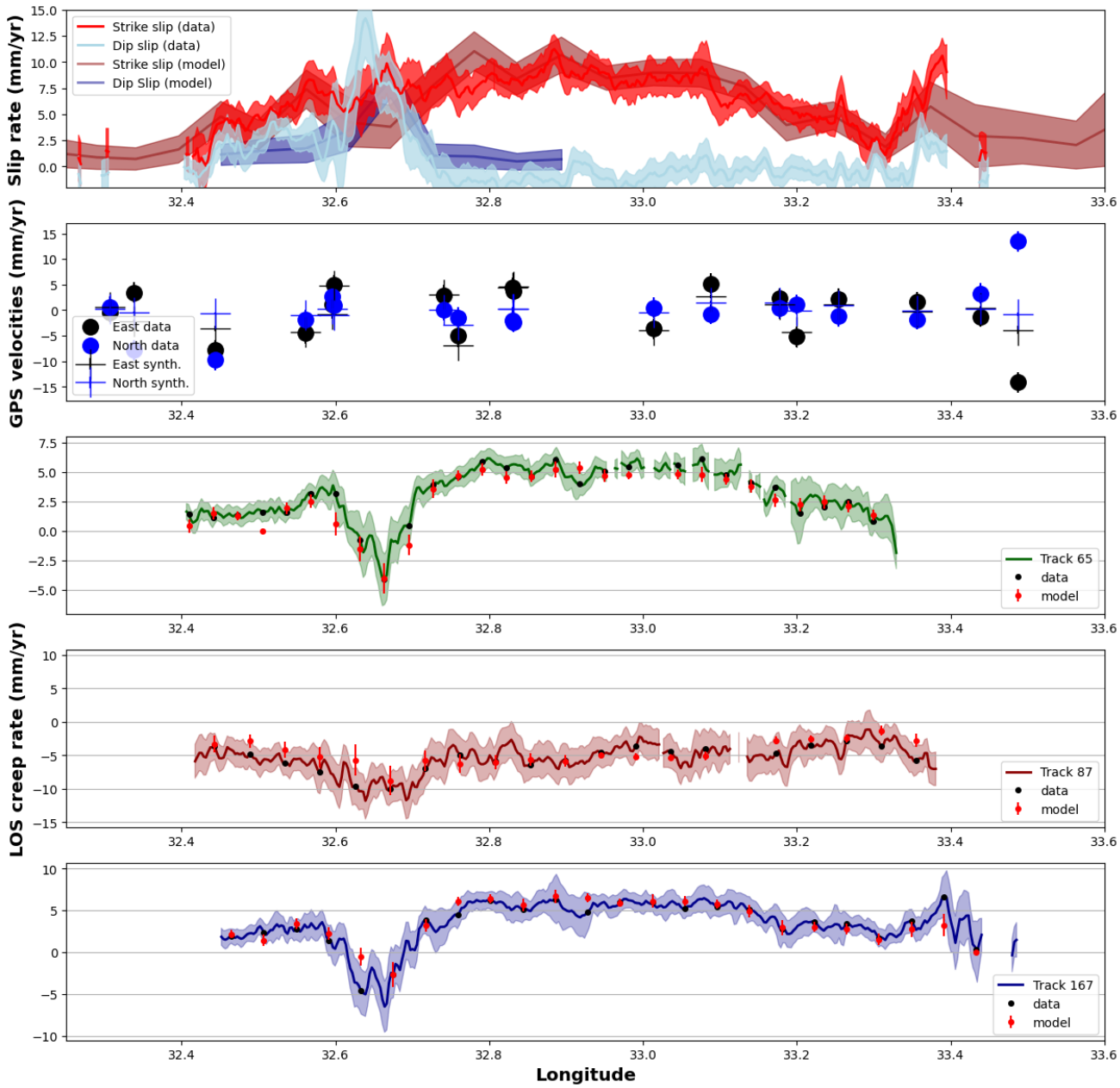

Figure S-34. Fit to the surface fault slip data - Top Surface slip rate measured on the horizontal and vertical ground motion maps and surface slip rate from the posterior PDF of the slip rate model. Red is for strike slip and blue for vertical differential motion (i.e. dip slip). **Second** Data (circles) and predictions from the mean model (crosses) for the GNSS data along the fault in the east (black) and north (blue) directions. **Three bottom plots** Data (lines) and predictions from the mean model for the surface slip measured on InSAR velocity maps.

4. Slip rates at Ismetpasa

All slip rates from table S-3 were measured within a short distance from the city of Ismetpasa. Most of these measurements were made within the city, at the train station, while some of them average over a distance difficult to estimate, depending on the publication. Refer to Bilham et al. (2016) for a detailed description of these surface slip rates. Rates are from Ambraseys (1970), Aytun (1982), Eren (1984), Deniz et al. (1993), Altay and Sav (1991), Çakir, Akoglu, Belabbes, Ergintav, and Meghraoui (2005), Kutoglu and Akcin (2006), Kutoglu, Akcin, Kemaldere, and Gormus (2008), Kutoglu, Akcin, Gundogdu, Gormus, and Koksal (2010), Karabacak, Altunel, and Cakir (2011), Deguchi (2011), Ozener, Dogru, and Turgut (2013) and Kaneko, Fialko, Sandwell, Tong, and Furuya (2012). Some rates were re-evaluated by Bilham et al. (2016). We have manually digitized figure 5 of Altay and Sav (1991).

Time	**Creep rate mm/yr**	**Std dev mm/yr**	**Observation Period start - end**	**Source**	**Measurement type**
1963	10.40	0.40	1957-1969	Ambraseys (1970)	Wall offset (photo)
1975	10.80	0.40	1969-1979	Aytun (1982)	Triangulation
1977	10.20	0.60	1972-1979	Eren (1984)	Trilateration
1987	9.30	0.70	1982-1992	Deniz et al. (1993)	Trilateration
1997	7.80	0.50	1992-2002	Kutoglu and Akcin (2006)	GNSS
1986	7.30	0.10	1982-1990	Altay and Sav (1991)	Creepmeter
2004	12.00	1.30	2002-2007	Kutoglu et al. (2008)	GNSS
2007	15.10	4.10	2007-2008	Kutoglu et al. (2010)	GNSS
1996	8.00	3.00	1992-2001	Çakir et al. (2005)	InSAR
2008	8.35	0.24	2003-2011	Cetin et al. (2014)	InSAR
2009	8.40	1.60	2007-2009	Karabacak et al. (2011)	LiDAR
2008	7.60	1.10	2005-2011	Ozener et al. (2013)	GNSS
2009	9.00	1.00	2007-2011	Kaneko et al. (2013)	InSAR
1992	8.30	0.10	1969-2016	Bilham et al. (2016)	Wall offset
1999	7.10	0.30	1984-2016	Bilham et al. (2016)	Wall offset
1976	9.90	0.30	1969-1984	Bilham et al. (2016)	Wall offset (photo)
2015	5.90	0.10	2014-2016	Bilham et al. (2016)	Creepmeter
2015	6.10	1.00	2014-2016	Bilham et al. (2016)	Wall offset
2017	6.00	2.00	2014-2021	This study	S1 InSAR

Table S-3: **Slip rates at Ismetpasa -** Table of slip rates measured at Ismetpasa since the 1950's. Please be aware that this table is almost entirely a copy of that from Bilham et al 2016 and this paper should be cited whenever this table is used.

5. Effect of model parameterization

We have tested the influence of the discretization of the dislocations at depth, below the brittle ductile transition. The model shown in the main text includes 70 km-wide, along strike, dislocations. Here, we show the mean of the a posteriori PDF for dislocations of 10, 20, 40 and 70 km-wide along strike. We do not observe significantly different slip patterns along the shallow section of the fault and, while slip rate increase within the patch located at depth with thinner dislocations, the misfit does not improve significantly, the deep slip rate remains similar and uncertainties on the shallow slip rate distribution increase significantly.

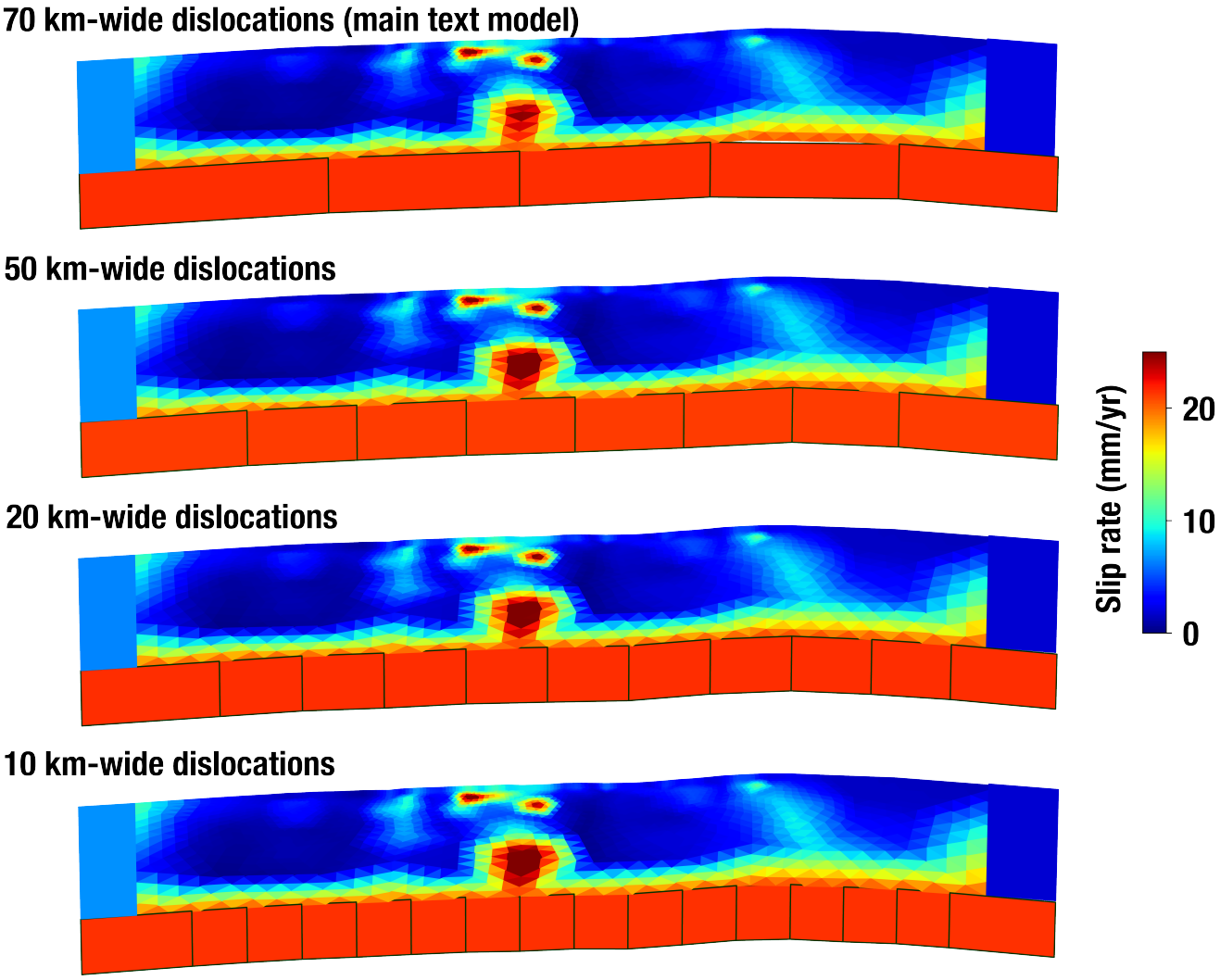

Figure S-35. Comparison between different model parameterization - Top to bottom Mean of the a posteriori PDF for different along strike width of deep dislocations. From top to bottom, dislocation width decreases from 70 to 40, 20 and 10 km. The pattern of slip rate along the shallow portion of the fault remains comparable and the conclusions remain unchanged.

References

Altay, C., & Sav, H. (1991). Continuous creep measurement along the North Anatolian Fault zone. *Bulletin of the geological congres of Turkey*, *6*, 77–84.

Ambraseys, N. N. (1970). Some characteristic features of the Anatolian fault zone. *Tectonophysics*, *9*, 143–165.

Aytun, A. (1982). Creep Measurements in the Ismetpaşa Region of the North Anatolian Fault Zone. *Multidisciplinary Approach to Earthquake Prediction Progress in Earthquake Prediction Research*, *2*, 279–292.

Bilham, R., Ozener, H., Mencin, D., Dogru, A., Ergintav, S., Çakir, Z., ... Mattioli, G. (2016). Surface creep on the North Anatolian Fault at Ismetpasa, Turkey, 1944-2016. *Journal of Geophysical Research-Solid Earth*, *121*, 7409– 7431. doi: 10.1002/2016JB013394

Çakir, Z., Akoglu, A., Belabbes, S., Ergintav, S., & Meghraoui, M. (2005). Creeping along the Ismetpasa section of the North Anatolian fault (Western Turkey): Rate and extent from InSAR. *Earth and Planetary Science Letters*, *238*(1-2), 225–234. doi: 10.1016/j.epsl.2005.06.044

Deguchi. (2011). Detection of fault creep around naf by insar time series analysis using palsar data. *Proc. of SPIE, SAR Image Analysis, Modeling, and Techniques XI*, *8179*. doi: 10.1117/12.898478

Deniz, R., Aksoy, A., Yalin, D., Seeger, H., Franke, P., Hirsch, O., & Bautsch, P. (1993). Determination of crustal movements in turkey by terrestrial geodetic methods. *Journal of Geodynamics*, *18*(1), 13–22. doi: 10.1016/0264-3707(93)90024-Z

Eren, K. (1984). Strain analysis along the north analtolian fault by using geodetic surveys. *Bulletin géodésique*, *58*(2), 137–150. doi: 10.1007/BF02520898

Kaneko, Y., Fialko, Y., Sandwell, D. T., Tong, X., & Furuya, M. (2012). Interseismic deformation and creep along the central section of the North Anatolian fault (Turkey): InSAR observations and implications for rate-and-state friction properties. *Journal of Geophysical Research-Solid Earth*, *118*, 316– 331. doi: 10.1029/2012JB009661

Karabacak, V., Altunel, E., & Cakir, Z. (2011). Monitoring aseismic surface creep along the north anatolian fault (turkey) using ground-based lidar. *Earth and Planetary Science Letters*, *304*(1), 64–70. doi: 10.1016/j.epsl.2011.01.017

Kutoglu, H. S., & Akcin, H. (2006). Determination of the 30-year creep trend on the ismetpaşa segment of the north anatolian fault using an old geodetic network. *Earth, Planets and Space*, *58*(8), 937–942. doi: 10.1186/BF03352598

Kutoglu, H. S., Akcin, H., Gundogdu, O., Gormus, K. S., & Koksal, E. (2010, 12). Relaxation on the ismetpasa segment of the north anatolian fault after the golcuk $m_w = 7.4$ and duzce $m_w = 7.2$ shocks. *Nat. Hazards Earth Syst. Sci.*, *10*(12), 2653–2657. doi: 10.5194/nhess-10-2653-2010

Kutoglu, H. S., Akcin, H., Kemaldere, H., & Gormus, K. S. (2008, 12). Triggered creep rate on the ismetpasa segment of the north anatolian fault. *Nat. Hazards Earth Syst. Sci.*, *8*(6), 1369–1373. doi: 10.5194/nhess-8-1369-2008

Ozener, H., Dogru, A., & Turgut, B. (2013). Quantifying aseismic creep on the ismetpasa segment of the north anatolian fault zone (turkey) by 6 years of gps observations. *Journal of Geodynamics*, *67*, 72–77. doi: 10.1016/j.jog.2012.08.002